sustainability

MDPI

Article

Spatial and Temporal Analysis of Climatic Precursors before Major Earthquakes in Iran (2011–2021)

Mohammad Reza Mansouri Daneshvar [1,*], Friedemann T. Freund [2] and Majid Ebrahimi [3]

[1] Department of Geography and Natural Hazards, Research Institute SP, Mashhad 91978-75699, Iran
[2] SETI Institute, 339 N Bernardo Ave Suite 200, Mountain View, CA 94043, USA; ffreund@seti.org
[3] Department of Physical Geography, Hakim Sabzevari University, Sabzevar 96179-76487, Iran
* Correspondence: mrm_daneshvar2012@yahoo.com

Abstract: The present study provides a systematic assessment of the relationships between climatic variables and major earthquakes (M > 6) in Iran (2011–2021). These variables include total cloud cover (tcc), low cloud cover (lcc), total precipitation (tp), surface latent heat flux (slhf), and total column rainwater (tcrw). Based on a wider set of variables provided by a multidimensional global dataset (ERA5), the combination of a cross-correlation function (CCF) and receiver operating characteristic (ROC) was used to develop the spatial and temporal analytic relations. Covering maximal values from 0.42 to 0.92, the CCF plots revealed that an increase in climatic parameters could provide valuable information about impending earthquake activity within 8 to 20 days. The mean values of tcc, lcc, tp, slhf, and tcrw were found to increase by 95%, 60%, 80.0 mm, 105 W/m^2, and 95 kg^{-3}/m^2, respectively. In fact, with the mean AUC (area under the curve) indices ranging from 0.677 (tcc) to 0.810 (tcrw) prior to major earthquakes, the ROC plots allowed for discrimination between seismic and climatic variables ranging from "acceptable" to "excellent". The changes in the climatic variables under study were due to anomalous air ionization and water condensation in the atmosphere, which can be regarded as short-term precursors to major earthquakes.

Keywords: climatic variables; cross-correlation; earthquake events; spatial analysis; time series; Iran

Citation: Mansouri Daneshvar, M.R.; Freund, F.T.; Ebrahimi, M. Spatial and Temporal Analysis of Climatic Precursors before Major Earthquakes in Iran (2011–2021). *Sustainability* **2023**, *15*, 11023. https://doi.org/10.3390/su151411023

Academic Editor: Sotirios Argyroudis

Received: 1 May 2023
Revised: 28 June 2023
Accepted: 4 July 2023
Published: 14 July 2023

1. Introduction

Earth is a tectonically active planet. Sections of the rigid crust, known as "plates", slowly drift across the Earth's surface, pushed and pulled by large-scale mass convections in the Earth's mantle. As a result of these movements, sections of the plates rub against each other, slide past each other, and/or collide. On a microscopic scale, the tectonic stresses cause mineral grains to shift along grain boundaries and to deform through dislocation movements. The picture that emerges here falls into the realm of mechanical physics.

However, in seismically active regions, tectonically induced dynamic stresses were also widely reported to lead to anomalous electromagnetic emissions over a wide frequency range (e.g., [1,2]). Prior to major earthquakes, several climatic parameters seemed to quickly or gradually change within a given time window—events that are typically called "earthquake precursors" [3]. Recent studies of the lithosphere and atmosphere coupling, as part of the global earthquake forecasting system [4], suggested triggering processes for the observable atmospheric anomalies between the ground level and upper atmospheric levels [5]. Despite some "up-down" evidence regarding solar activity before some large earthquakes (e.g., [6]), our hypothesis, concerning the link between climate and earthquakes, is a triggering mechanism influenced by positive holes at the ground-to-air interface, which can be a result of seismic/tectonic processes at depth, i.e., a "bottom-up" process, as defined by Freund [7–9]. This was described as the field ionization of the air molecules at the Earth's surface.

Some scholars explain the field ionization of air as occurring due to the enhanced radon gas emanation along faults (see [10–13]). An alternative explanation based on the

peroxy defect theory (see [8,9,14]) assigns air ionization to the formation of microscopic but very steep electric field gradients at the surface of the Earth, which occur due to the arrival of highly mobile electronic charge carriers. Regardless of which of the two explanations best describes the cause of the anomalous air ionization at the Earth's surface, it is by now well-established that an increase in the tectonic stresses in the Earth's crust prior to major seismic events leads to atmospheric and ionospheric anomalies over the affected areas. Indeed, numerous studies provided evidence of climatic abnormalities before major earthquakes (e.g., [3,15–38]). Many of these studies focused on satellite data, because remote sensing offers distinct advantages over traditional approaches based on ground stations including global coverage and high spatial–temporal resolution [37]. Earthquake precursors derived from space-based observations, therefore, provided excellent insights into preseismic anomalies over epicentral regions [38]. Many scholars reported persistent and simultaneous anomalies in different observable parameters prior to major earthquakes [39].

For the area of Iran, various climatic precursors prior to major earthquakes were reported by Daneshvar and colleagues [40–44]. Despite the notable results in the previous studies, the lack of any comprehensive multiparametric investigations regarding the climatic anomalies before earthquake events is a research gap in Iran. The present study attempts to fill this gap by considering a systematic assessment of the relations between different climatic variables and major earthquakes covering the decade of 2011–2021, using time series of approximately 30 days before major seismic events. The work presented here aims to discover multi-disciplinary pre-earthquake signals by selecting several climatic variables and using an international dataset (ERA5) with broad spatial and temporal coverage. The study combines a cross-correlation function (CCF) with receiver operating characteristics (ROC).

2. Study Area

The region between 25–40° north latitude and 44–64° east longitude was selected as the study area, comprising the country of Iran (Figure 1). Iran is situated in one of the most seismically active regions in the world, due to interactions between the Eurasian and African plates, including subduction zones, active transform faulting, crustal compression, and extension [40,44]. The regional climate of Iran is controlled by diverse topographical features (with elevation ranging from –56 to 5415 m a.s.l), including an arid zone in the central plateau of Iran surrounded by two semi-arid mountain regions, including the Alborz in the north and the Zagros in the west [45]. According to world climate data, the mean annual temperature and precipitation range from 16 °C to 20 °C and from 200 mm to 400 mm, respectively [46].

Using historical earthquake data and information about geology, tectonics, and fault activity, Daneshvar et al. [47] divided Iran's surface area into six major seismic regions. They included the Makran (i) along the active subduction of the Arabia plate beneath the Eurasia plate, the folded Zagros Mountains (ii), the mountains of Alborz (iii), and the Kopet Dagh (iv), in addition to Central Iran (v) and the Kerman region (vi), formed by strike-slip and reverse faults. Across these seismological regions of Iran, 17 major earthquakes with magnitude > 6 on the Richter scale occurred during the decade of 2011–2021. Relevant data were obtained from the global earthquake archive of the United States Geological Survey (https://earthquake.usgs.gov/earthquakes/search, accessed on 20 December 2022) [48]. Among the selected 17 major earthquakes, exactly 2, 8, 2, 1, and 4 events occurred in the active regions of Makran, Zagros, Alborz, Kopet Dagh, and Kerman, respectively. They occurred in 13 distinctive time windows and 12 geographical regions. Hence, the cases presented here comprise 13 earthquake dates and 12 epicenter locations. The geographical coordinates, dates, and characteristics of these major earthquakes are given in Table 1. In the same time period of 2011–2021, approximately 2410 earthquakes occurred in Iran with a magnitude > 4.

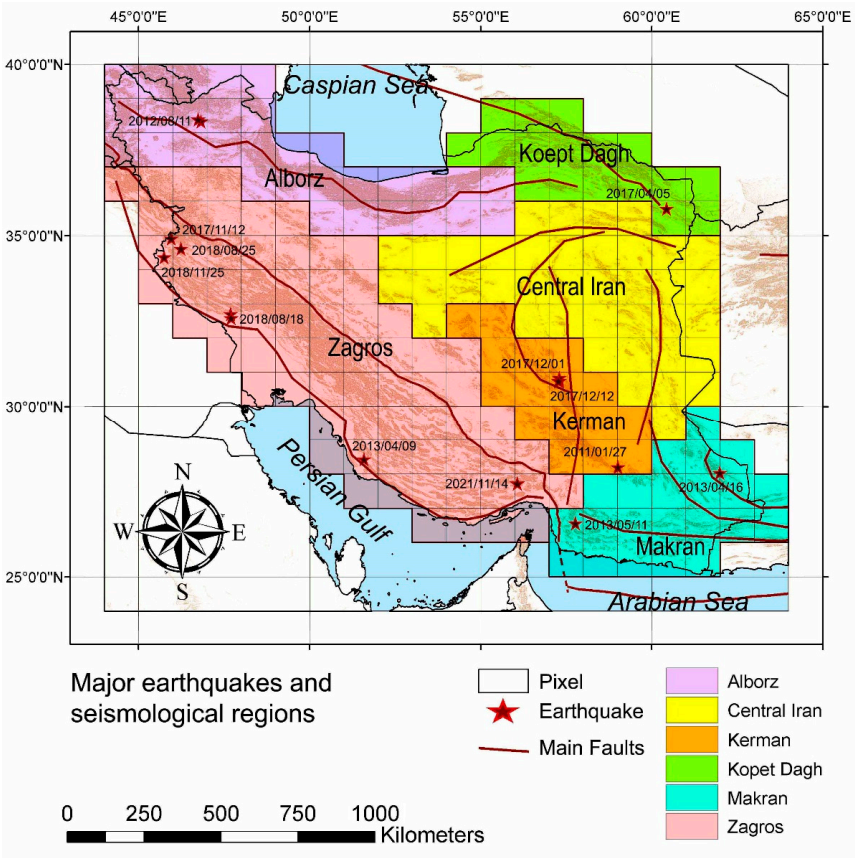

Figure 1. Map of the study area for the M > 6 earthquakes in 2011–2021 in different seismically active regions of Iran. (Note: In the Makran region, the greenish-blue color extends beyond the coastline.)

Table 1. Geographical positions, dates, and physical characteristics of the major earthquakes in Iran during 2011–2021.

Earthquake Date	Latitude (°)	Longitude (°)	Depth (km)	Magnitude (Richter)	Faulting Mechanism *	Seismological Region
27 January 2011	28.20	59.02	10	6.2	Strike slip	Kerman
11 August 2012	38.33	46.83	11	6.4	Strike slip	Alborz
11 August 2012	38.39	46.75	12	6.2	Strike slip	Alborz
9 April 2013	28.43	51.59	12	6.4	Strike slip	Zagros
16 April 2013	28.03	62.00	80	7.7	Normal dip slip	Makran
11 May 2013	26.56	57.77	15	6.1	Strike slip	Makran
18 August 2014	32.70	47.70	10	6.2	Compressional	Zagros
18 August 2014	32.58	47.70	5	6.0	Compressional	Zagros
5 April 2017	35.78	60.44	13	6.1	Strike slip	Kopet Dagh
12 November 2017	34.91	45.96	19	7.3	Compressional	Zagros
1 December 2017	30.75	57.31	9	6.1	Thrust	Kerman
12 December 2017	30.83	57.30	8	6.0	Thrust	Kerman
12 December 2017	30.74	57.28	12	6.0	Thrust	Kerman
25 August 2018	34.61	46.24	10	6.0	Strike slip	Zagros
25 November 2018	34.36	45.74	18	6.3	Strike slip	Zagros
14 November 2021	27.73	56.07	10	6.4	Thrust	Zagros
14 November 2021	27.72	56.07	9	6.0	Thrust	Zagros

*: Faulting mechanism of earthquake events obtained from technical reports produced by the International Institute of Earthquake Engineering and Seismology (http://www.iiees.ac.ir/en, accessed on 25 December 2022).

3. Data and Methods

3.1. Data Preparation

The main goal of this work is to study the relationship between climatic variables and earthquake events in Iran. While prior research focused on a few variables such as precipitation and temperature, this study aims at identifying all effective variables out of the 340 surface and single-level parameters in the ERA5 (European Centre for Medium-Range Weather Forecasts reanalysis data version 5) database from the European Copernicus Climate Change Service and Climate Data Store (https://cds.climate.copernicus.eu/cdsapp#!/dataset/reanalysis-era5-single-levels, accessed on 20 December 2022) [49]. Hence, for the pre-earthquake analysis in Iran, this work uses the database of global ERA5 hourly and daily data. This database was extensively mined using a multidimensional NetCDF (network common data form) format of the data in GIS (geographical information system) with an enlarged number of parameters, times, and locations.

The geospatial data extraction (climatic variables in hourly and daily time scales) was completed over the selected epicentral regions of each large earthquake, corresponding to a size of approximately $1^\circ \times 1^\circ$. According to the literature, different spatial resolutions are to be used to detect the non-seismic and atmospheric perturbations before large earthquake events over their respective epicenter regions, which are mostly constrained by the resolution of the atmospheric data used such as a spatial mesh of $1^\circ \times 1^\circ$ [3]. The spatial mesh covering Iran with a geographical grid of $1^\circ \times 1^\circ$ includes 194 pixels [47].

Using a spatial mesh of 194 geographical pixels for 17 major earthquake events, the relations between 340 climatic variables (pointed out in the ERA5 database) were analyzed within their respective time series (within a mean of 30 days) only before their main shocks. After performing a skimming process in GIS for each major earthquake based on certain changes before each major earthquake (i.e., the anomaly of the standard deviation of data variations from the long-term average [16]), it was recognized that five variables possess sufficient quality to reveal a dependency on the earthquake events in Iran: (i): low cloud cover (lcc), (ii): total cloud cover (tcc), (iii): total precipitation (tp), (iv): surface latent heat flux (slhf), and (v): total column rainwater (tcrw). These variables were selected based on at least one recorded anomaly in at least one of the monthly time series data. Here, "anomaly" is defined as a deviation of data beyond the upper or lower confidence limits of the reference values. In each time series, the long-term average value of the same periods during 2011–2021 was defined as the reference value.

Under those conditions, (i): low cloud cover (lcc) is the proportion of clouds in the lower tropospheric levels, expressed as percentage (%); (ii): the total cloud cover (tcc) is the percentage (%) of grid pixels covered by clouds; (iii): the total precipitation (tp) is the accumulated liquid and frozen water, e.g., rain and snow, which falls to the Earth's surface, expressed in millimeters (mm); (iv): the surface latent heat flux (slhf), given in watts per square meter (W/m^2), is the transfer of latent heat (resulting from water phase changes such as evaporation or condensation) between the Earth's surface and the atmosphere through the effect of turbulent air motions; and (v): the total column rainwater (tcrw) in kilograms per square meter(kg/m^2) $\times 10^{-3}$, is defined as the total amount of rain that falls as precipitation in a column extending from the surface of the Earth to the top of the atmosphere. All variables mentioned here were estimated over a daily time coverage and geographical $1^\circ \times 1^\circ$ grid using the multidimensional NetCDF files of the ERA5 database.

3.2. Data Analysis

The present study considers a specific methodology to investigate the relations between climatic variables and major earthquake events within the time series (~30 days) only before the main shocks. As mentioned in the previous section, the earthquake data were obtained from the United States Geological Survey [48], comprised of major earthquakes ($M > 6$) and other tectonic shocks ($M > 4$) for each epicenter location within a 30-day time series. The events that are $4 < M < 6$ can be dominantly observed as aftershocks and rarely as foreshocks. Previously, research revealed the overall relationships between precipitation

rates and the frequency of earthquakes at the country scale of Iran [44]. Meanwhile, another study [35] revealed the relationships between precipitation anomaly and the frequency of the aftershocks in some major earthquakes (M > 6) in Japan. Hence, the frequency of all events is important, and the present study focused on the relationships between some climatic parameters and earthquake frequency over the epicenter location of each major earthquake, using CCF and ROC methods. Also, the frequency of the earthquake events (foreshocks or aftershocks) with M > 4 were represented in the research time series.

3.2.1. Cross-Correlation Function (CCF)

After preparing all five time series of the climatic variables in addition to one time series of the frequencies of earthquake events, a time-lagged correlation was applied, named "cross-correlation function" (CCF), which was developed for similar studies [44,50]. In the CCF test between two time series (earthquake event and climatic variables), the series of earthquake events are assumed as the influential input, and the climatic time series is called the affected outcome [51]. The pre-earthquake response of Earth's crust can occur over days, months, or years, while the associated stresses and their environmental impact can affect the entire ecosystem and climate (see [51–55]). Hence, the CCF between the time series of pre-earthquake precursors (i.e., climatic variables) and tectonic stresses can provide valuable insight into the chain of environmental changes within time. In this regard, the CCF method was estimated using SPSS (Statistical Package for Social Sciences) software under the tabs of "time series analysis" and "cross-correlation". The computations of the lagged time thresholds were assumed as the time lag number of ± 30 days for each selected earthquake (13 major earthquake cases) in Iran, and the time series values were extracted based on epicenter locations (geographical pixel of $1^\circ \times 1^\circ$).

First, a set of 65 CCF plots and matrices were produced for cross-correlations between five climatic variables and earthquake time series for 13 major earthquake cases. Second, the statistical results of CCF plots and matrices were averaged and combined as one plot and one table. In the combined plot and table, we can recognize a preceding time point (date) and preceding time interval (days) based on the time series, showing simultaneous precursory signals (anomalous increase or decline of climatic values) prior to the main shock of the major earthquakes.

3.2.2. Receiver Operating Characteristics (ROC)

After the time series was established, the relation between climatic precursory signals and earthquake events (with M > 4) was assessed. For this purpose, the area under the curve (AUC) of the receiver operating characteristic (ROC) was used based on the spatial mesh of 194 pixels in Iran (with a grid of $1^\circ \times 1^\circ$). In this method, which was categorized as the statistical discipline in the literature, e.g., [56], the overall performance of a relationship is drawn by plotting the "test variable" or specificity on the x-axis against the "actual state variable" or sensitivity on the y-axis in a ROC curve [57,58]. The ROC curves are then plotted under the "analyze" tab in SPSS. In these plots, the positive (=1) actual state of earthquake events is categorized as values ≥ 1 event, and the negative (=0) actual state is categorized as values = 0 (without event) in each spatial grid ($1^\circ \times 1^\circ$) over the country of Iran. In addition, positive and negative values of the test variables (climatic variables) are categorized as high values (meaning "valid") and low values (meaning "null"), respectively. According to the ROC plots, the area under the curve (AUC) is the most commonly used index, defining the probability of the relations between "actual state" and "test" variables with the average specificity toward sensitivity values. Acceptable and excellent discriminating values for the test variable mean AUC > 0.6, whereas poor and random values mean AUC < 0.6 [56,59]. In the present study, the AUC indices are used to examine the research aim, regarding the relation between climatic precursory signals and earthquake events.

4. Results and Discussion

4.1. Estimation of CCF

As mentioned in the above sections, the CCF method recognizes a preceding time point (date) and preceding time interval (days) based on the time series, in which the climatic variables represent simultaneous precursory signals, as an anomalous increase or decrease in values, prior to the main shock of the major earthquakes. In this regard, the application of cross-correlations suggests that the input signal refers to an atmospheric or climate parameter, while the output signal refers to a state of the Earth's crust, i.e., an earthquake event [44]. In this regard, daily time-lagged correlation coefficients between earthquake events and variations of five climatic variables were produced through 65 matrices and plots. The CCF coefficients are assumed as the average values in Table 2. They reveal upper CCF values ranging from 0.42 to 0.92, indicating significant correlations above the upper confidence limit at 90%. Bold digits relate to the maximum coefficients of the cross-correlation function, representing the time before the major earthquakes considered in this study.

Consequently, the mean daily time-lagged correlations between earthquakes and effective climatic time series in Iran (2011–2021) are summarized in the CCF plot in Figure 2, showing estimated time lags. Based on ±30 days (time lag number), the cross-correlation functions revealed a positive link between the climatic and earthquake time series with the anticipant time lags from 1 day to 20 days. In other words, the high values of the climatic variables for low cloud cover (lcc) conditions, total cloud cover (tcc) conditions, total precipitation (tp) conditions, surface latent heat flux (slhf) conditions, and total column rainwater (tcrw) conditions can be considered anomalous, pointing to impending major earthquake events (M > 6) within the next 20 days. The results of this CCF plot indicate that, when climatic parameters such as precipitation and surface latent heat flux increase, they forecast earthquake activity within the 8-day and 20-day time windows (p > 90%) that were found during previous studies such as in [3,20,40,43,44].

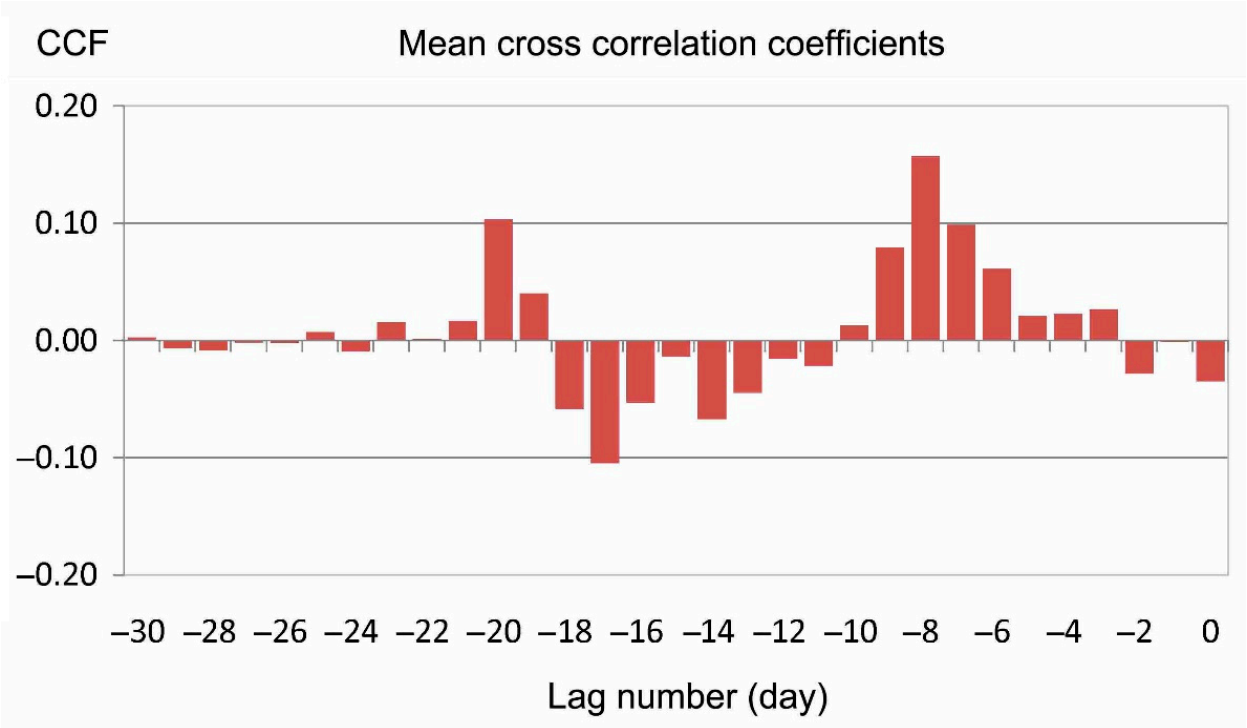

Figure 2. Mean daily time-lagged correlation test between major earthquake and effective climatic time series in Iran (2011–2021).

Table 2. Daily time-lagged correlation coefficients between major earthquake events and mean variation of 5 climatic variables.

Lag (day)	27 January 2011	11 August 2012	9 April 2013	16 April 2013	11 May 2013	18 August 2014	5 April 2017	12 November 2017	1 December 2017	12 December 2017	25 August 2018	25 November 2018	14 November 2021	Mean
−30	0.01	0.00	−0.01	0.00	0.01	0.00	0.01	0.00	0.01	0.01	0.00	0.00	0.01	0.00
−29	0.01	−0.01	−0.02	−0.01	0.00	0.01	0.01	−0.01	0.01	0.01	0.00	−0.10	0.01	−0.01
−28	0.02	0.01	−0.02	−0.02	0.01	0.01	0.01	−0.01	−0.01	0.02	−0.01	−0.13	0.01	−0.01
−27	0.02	−0.02	0.01	−0.01	0.00	0.01	0.02	−0.01	−0.09	0.02	0.01	0.00	0.01	0.00
−26	0.03	0.00	−0.01	−0.01	−0.02	0.01	0.00	−0.01	−0.08	0.03	−0.01	0.00	0.03	0.00
−25	0.04	0.00	0.04	−0.01	0.03	0.01	−0.02	−0.01	−0.07	0.03	0.09	−0.05	0.00	0.01
−24	0.03	0.02	0.02	0.01	0.00	0.01	−0.02	−0.02	−0.07	0.04	−0.10	−0.04	0.00	−0.01
−23	−0.01	0.05	0.03	0.16	0.03	0.01	−0.03	−0.05	−0.09	0.01	0.20	−0.09	−0.03	0.02
−22	−0.06	0.07	0.04	0.18	0.00	0.01	−0.03	−0.09	−0.13	−0.03	0.06	0.03	−0.02	0.00
−21	−0.13	0.23	0.19	−0.11	−0.09	0.01	−0.11	−0.08	−0.07	−0.09	0.30	0.23	−0.05	0.02
−20	−0.13	0.30	0.33	−0.12	−0.25	0.01	−0.14	−0.06	0.31	−0.10	0.78	0.49	−0.09	**0.10**
−19	−0.13	−0.10	−0.07	−0.10	−0.18	0.00	−0.14	−0.08	0.67	−0.09	0.34	0.47	−0.07	0.04
−18	−0.15	−0.14	−0.09	−0.13	−0.07	−0.04	−0.05	−0.10	0.45	−0.11	−0.15	−0.09	−0.09	−0.06
−17	−0.16	−0.10	−0.10	−0.11	−0.03	−0.04	0.02	−0.10	−0.19	−0.12	−0.15	−0.15	−0.13	−0.10
−16	−0.19	−0.09	−0.10	0.12	0.22	−0.04	0.27	−0.07	−0.21	−0.15	−0.14	−0.15	−0.15	−0.05
−15	−0.20	−0.06	−0.11	0.15	0.18	−0.05	0.61	−0.04	−0.11	−0.07	−0.14	−0.14	−0.20	−0.01
−14	−0.18	0.02	−0.14	−0.16	0.42	−0.11	−0.14	−0.01	−0.08	−0.01	−0.14	−0.17	−0.16	−0.07
−13	−0.18	0.06	−0.12	0.03	0.34	−0.11	−0.11	−0.04	−0.06	−0.02	−0.13	−0.10	−0.12	−0.04
−12	−0.11	0.57	−0.13	0.09	−0.05	−0.10	−0.03	0.00	−0.01	0.05	−0.13	−0.16	−0.20	−0.02
−11	0.05	0.55	−0.13	−0.13	−0.29	−0.07	0.00	−0.09	0.10	−0.01	−0.13	0.03	−0.16	−0.02
−10	0.29	−0.15	−0.08	0.28	−0.39	−0.05	0.45	−0.03	0.11	0.01	−0.12	−0.02	−0.12	0.01
−9	0.57	−0.14	−0.10	0.40	−0.37	−0.01	−0.13	0.04	0.20	0.40	−0.12	0.30	0.00	0.08
−8	0.55	−0.14	−0.01	0.79	−0.28	−0.06	−0.10	0.42	0.23	0.65	−0.12	−0.13	0.25	**0.16**
−7	0.38	−0.14	−0.07	−0.13	−0.01	−0.02	−0.07	0.32	0.14	0.52	−0.11	−0.14	0.62	**0.10**
−6	0.13	−0.13	0.00	−0.15	0.19	0.04	0.09	0.49	−0.13	−0.14	−0.11	−0.13	0.65	0.06
−5	−0.10	−0.13	0.10	−0.15	0.17	0.03	0.05	0.24	−0.12	−0.13	−0.11	−0.15	0.57	0.02
−4	−0.11	−0.13	0.35	−0.14	0.22	0.01	0.07	−0.12	−0.10	−0.05	−0.11	−0.09	0.48	0.02
−3	−0.13	−0.12	0.54	−0.14	0.29	0.09	0.06	−0.12	−0.12	−0.06	−0.11	−0.12	0.28	0.03
−2	−0.18	−0.12	−0.14	−0.13	0.18	0.46	0.08	−0.12	−0.12	−0.02	−0.11	0.07	−0.23	−0.03
−1	−0.15	−0.12	−0.04	−0.13	−0.02	0.92	0.05	−0.11	−0.08	−0.02	−0.10	0.06	−0.27	0.00
0	−0.09	−0.11	−0.08	−0.12	−0.13	0.20	−0.11	−0.09	−0.05	0.10	−0.06	0.34	−0.25	−0.03

Note: Bold digits represent maximum coefficients of the cross-correlation function, thereby probably preceding impending major earthquakes.

4.2. Analysis of Time Series

In Figures 3–14, some climatic time series are presented for 17 major earthquakes, reflecting the mean values of climatic variables of lcc, tcc, tp, slhf, and tcrw on 13 dates and at 12 epicenter locations. They, thus, confirm the abnormal but synchronous increase in climatic values during the 20 days prior to the main shocks. The prior dates and time intervals are based on the time-lagged correlation results. In addition, the mean values of five climatic variables during the prior date and time intervals (days) before major earthquakes are shown in Table 3 for the respective pixels (epicenter locations). For example, in the M6.2 earthquake on 27 January 2011, the preceding date was 19 January 2011, with a time interval of 9 days before the main shock (Figure 3). The mean climatic values reveal sudden increases in tcc, lcc, tp, slhf, and tcrw by 100%, 90%, 9.5 mm, 50 W/m^2, and 150 kg^{-3}/m^2, respectively. As another example, for the two earthquakes of M6.1 and M6.0 on 1 December 2017 and 12 December 2017, respectively, information about their approach was obtained on 23 November 2017 with 8 and 19 days of "warning" (Figure 11).

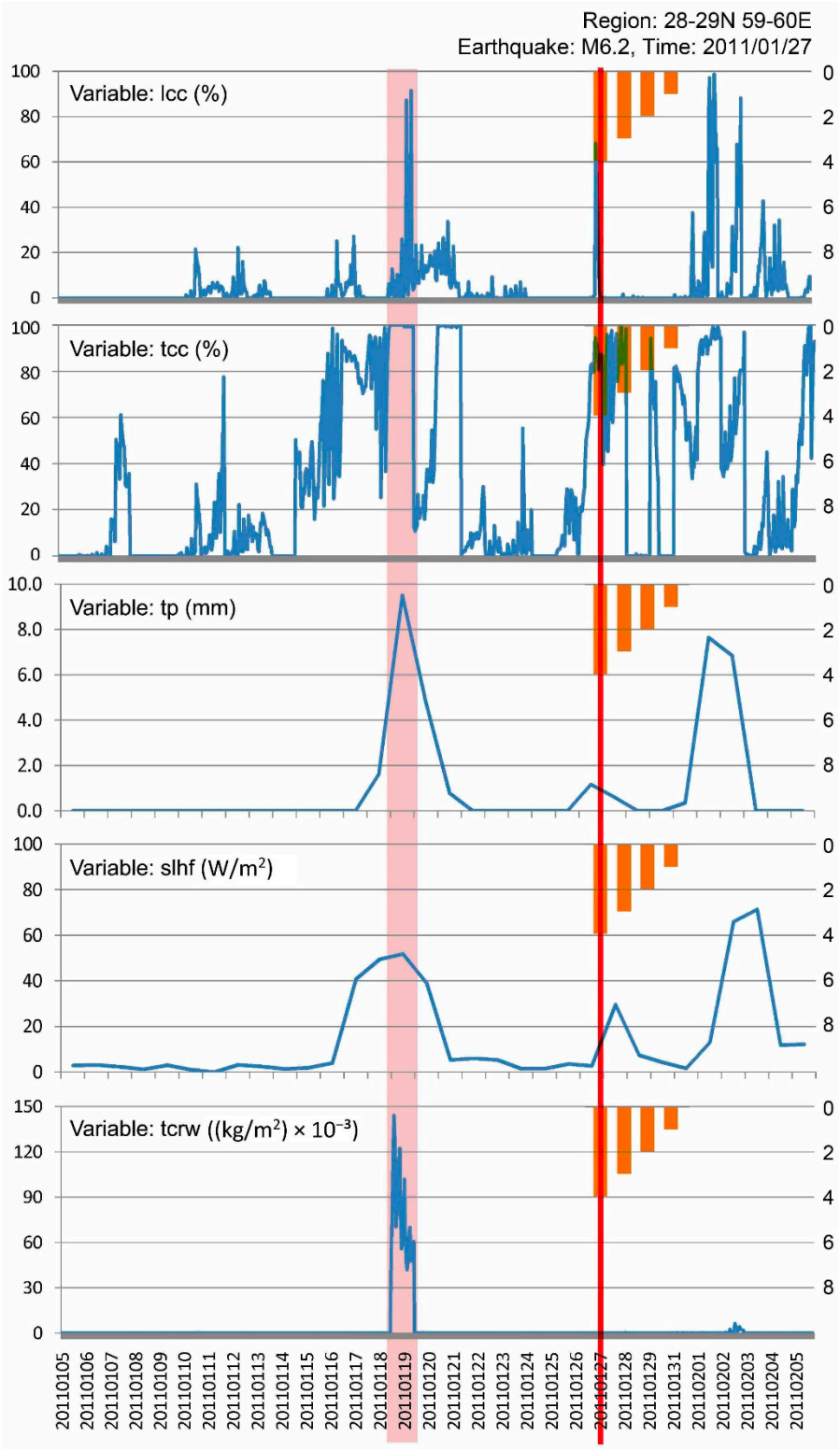

Figure 3. Time series for lcc, tcc, tp, slhf, and tcrw for the M6.2 earthquake on 27 January 2011 in the northeastern region of Iran (28–29° N, 59–60° E); pink strip represents the preceding date, red line shows the major earthquake date, and reverse orange columns are the frequency of the earthquake events (foreshocks or aftershocks) with M > 4 within the time series.

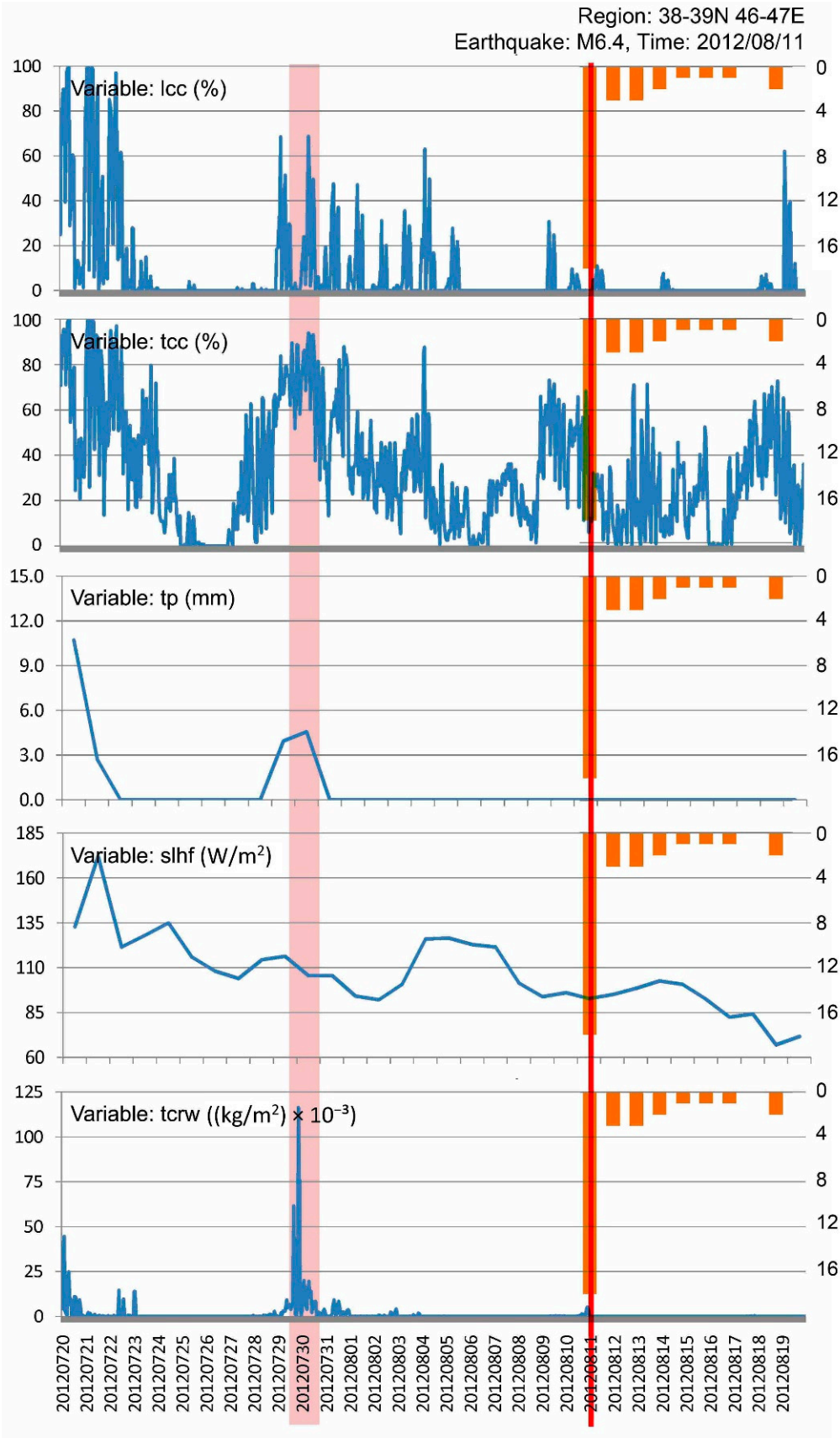

Figure 4. Climatic time series of lcc, tcc, tp, slhf, and tcrw for the M6.4 earthquake on 11 August 2012 in the northwestern region of Iran (38–39° N, 46–47° E).

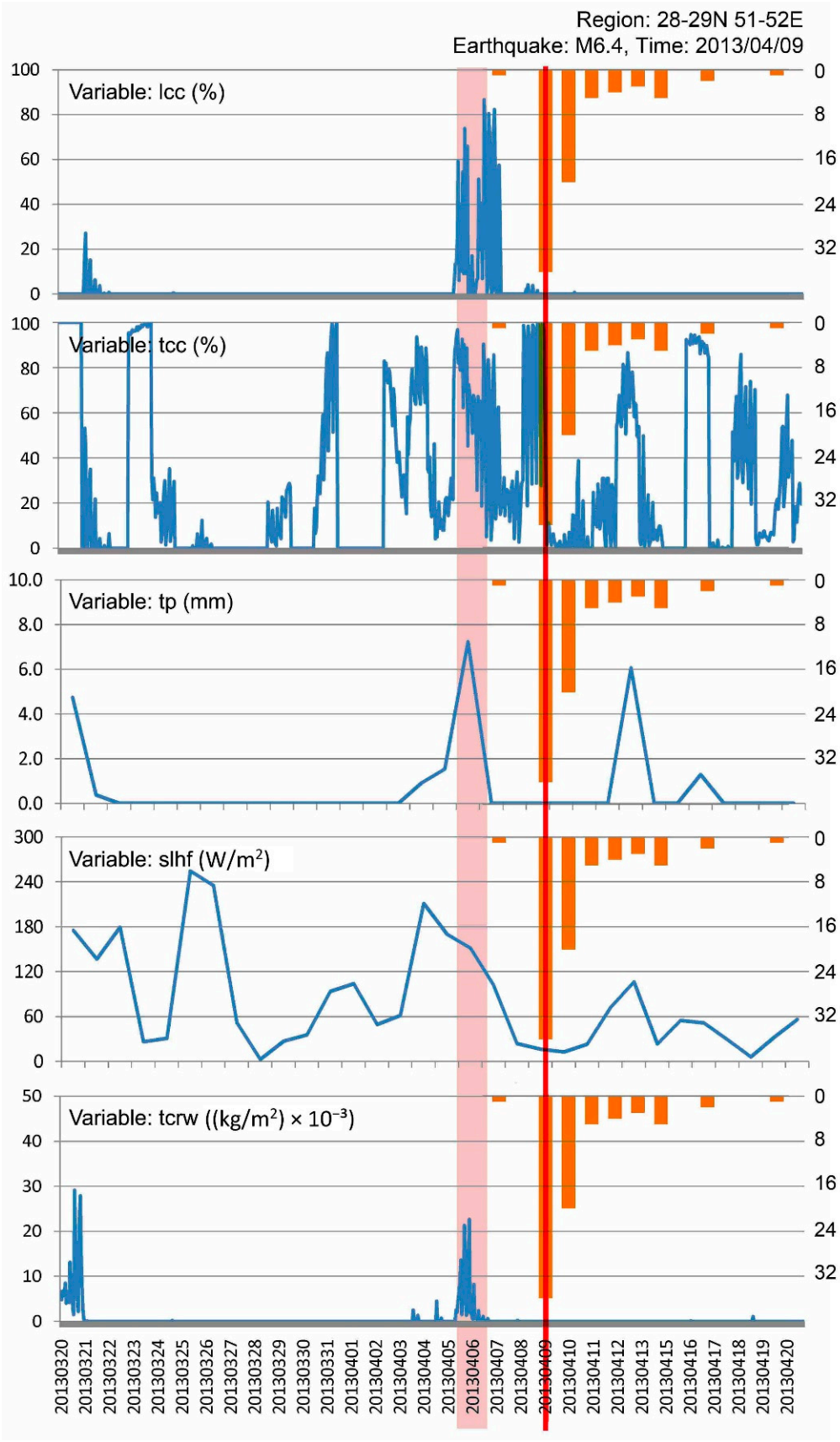

Figure 5. Climatic time series of lcc, tcc, tp, slhf, and tcrw for the M6.4 earthquake on 9 April 2013 in the southern part of Zagros (28–29° N, 51–52° E).

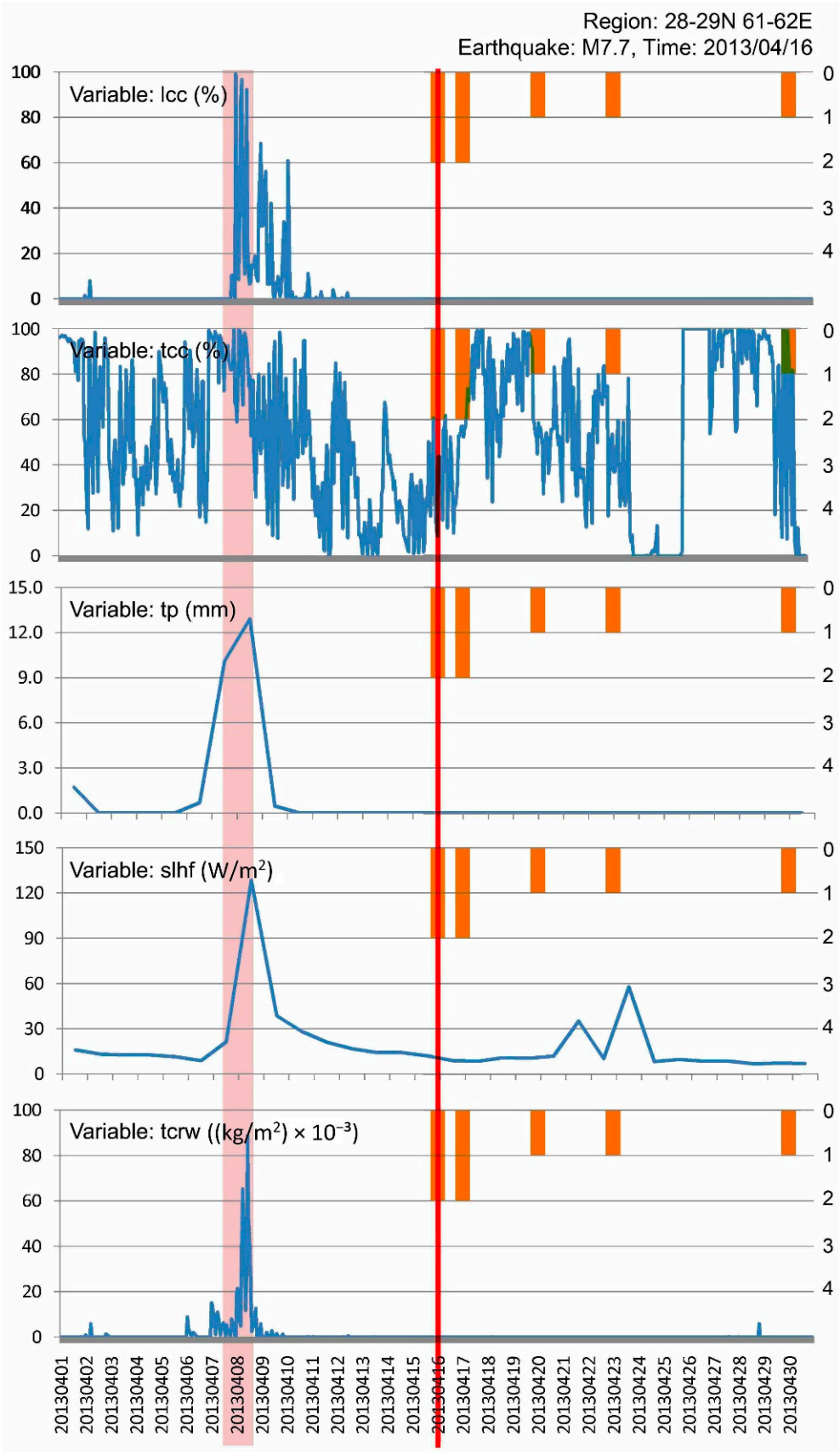

Figure 6. Climatic time series of lcc, tcc, tp, slhf, and tcrw for the M7.7 earthquake on 16 April 2013 in the southern part of Zagros (28–29° N, 61–62° E).

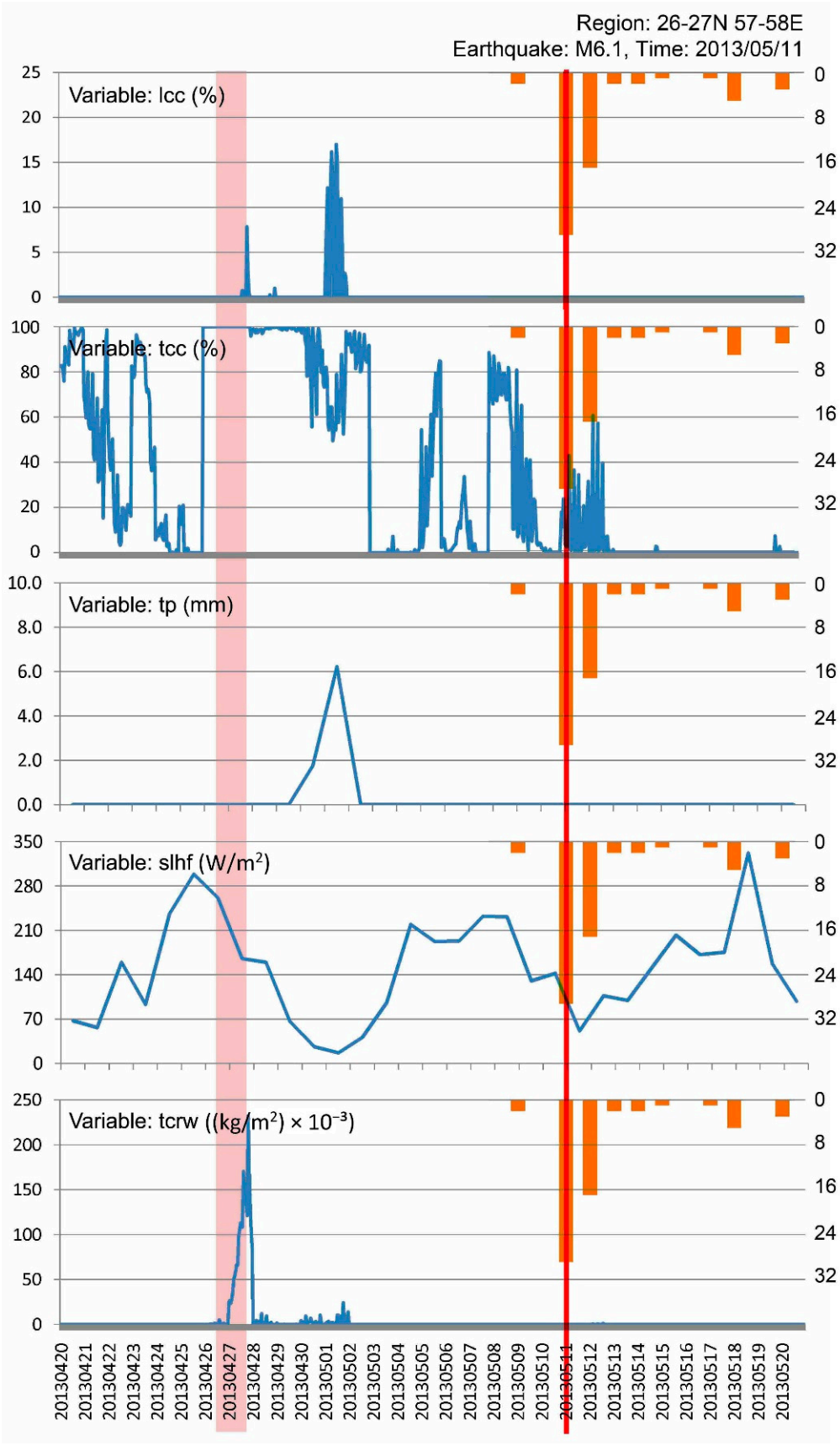

Figure 7. Climatic time series of lcc, tcc, tp, slhf, and tcrw for the M6.1 earthquake on 11 May 2013 in the southern part of Zagros (26–27° N, 57–58° E).

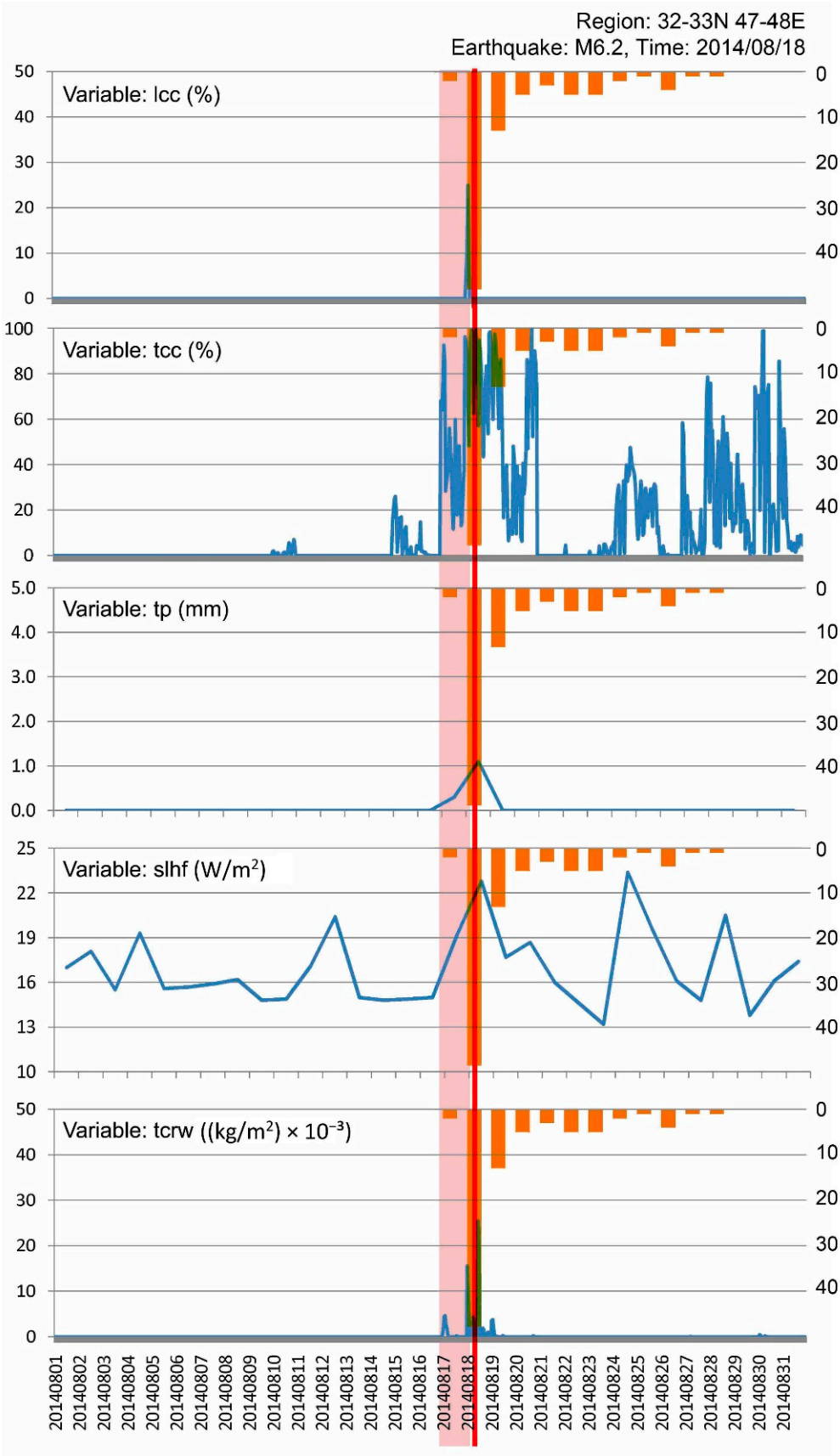

Figure 8. Climatic time series of lcc, tcc, tp, slhf, and tcrw for the M6.2 earthquake on 18 August 2014 in its seismological region (32–33° N, 47–48° E).

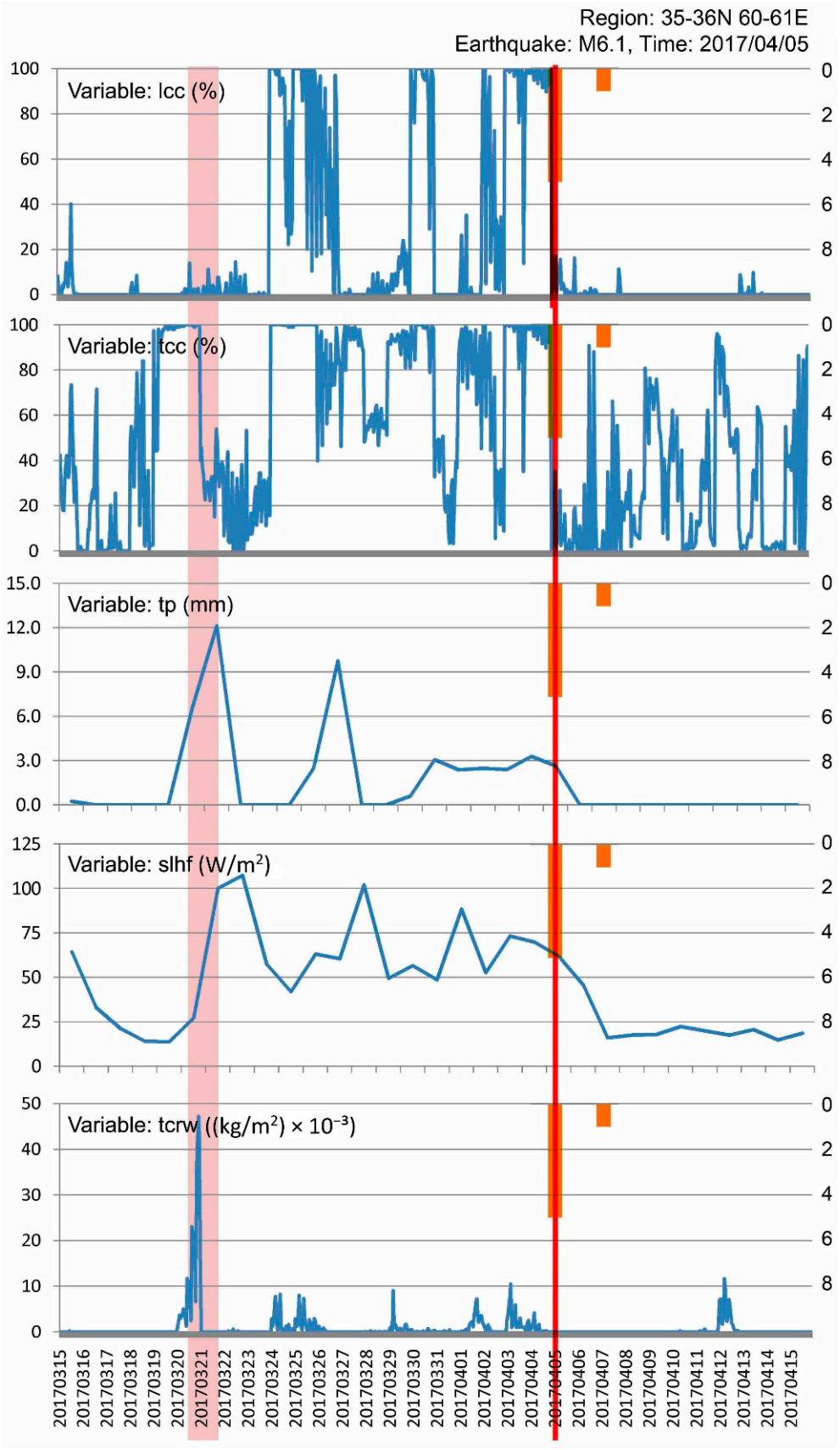

Figure 9. Climatic time series of lcc, tcc, tp, slhf, and tcrw for the M6.1 earthquake on 5 April 2017 in its seismological region (35–36° N, 60–61° E).

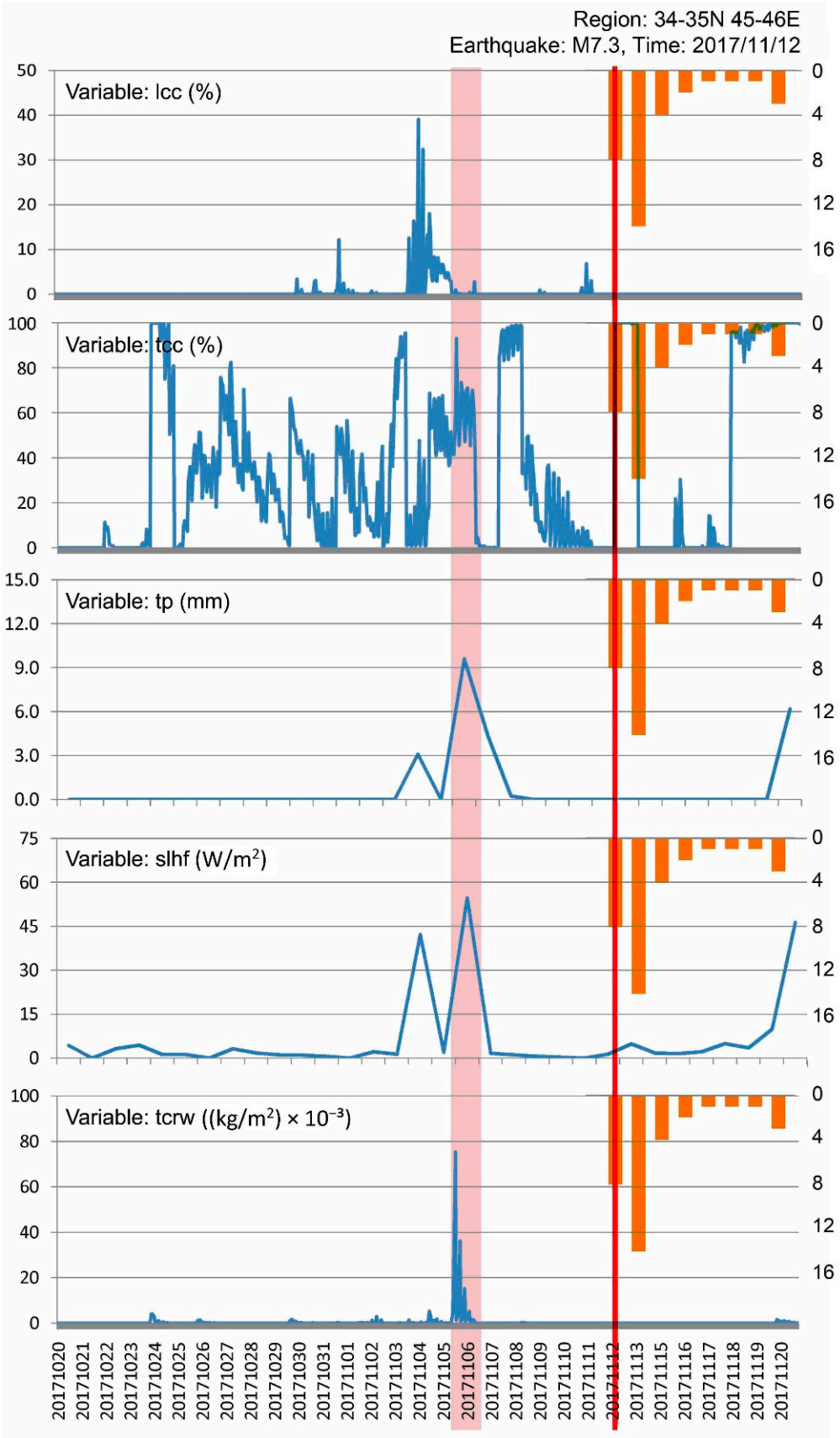

Figure 10. Climatic time series of lcc, tcc, tp, slhf, and tcrw for the M7.3 earthquake on 12 November 2017 in its seismological region (34–35° N, 45–46° E).

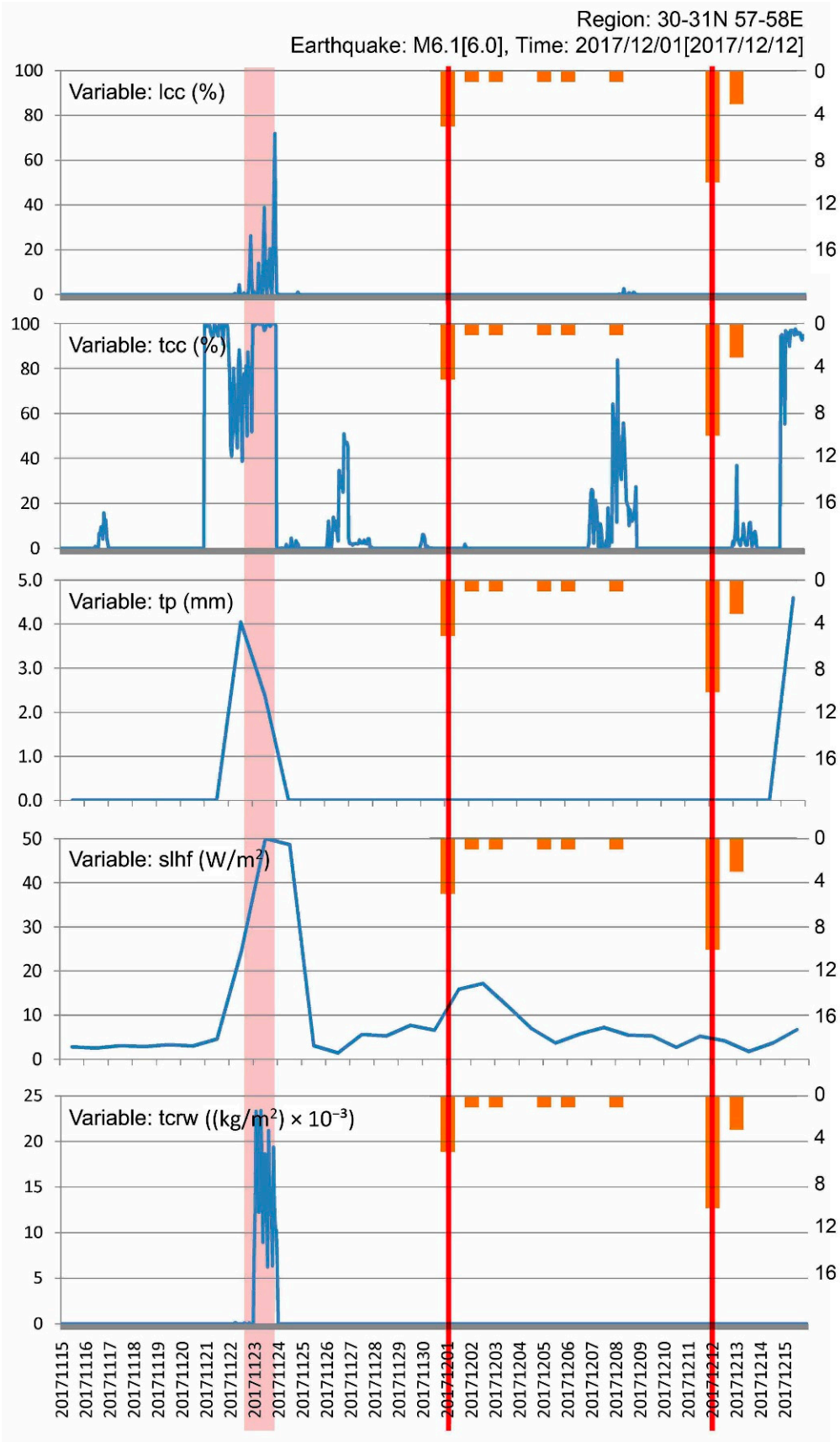

Figure 11. Climatic time series of lcc, tcc, tp, slhf, and tcrw for the M6.1 [M6.0] earthquake on 1 December 2017 [12 December 2017] in its seismological region (30–31° N, 57–58° E).

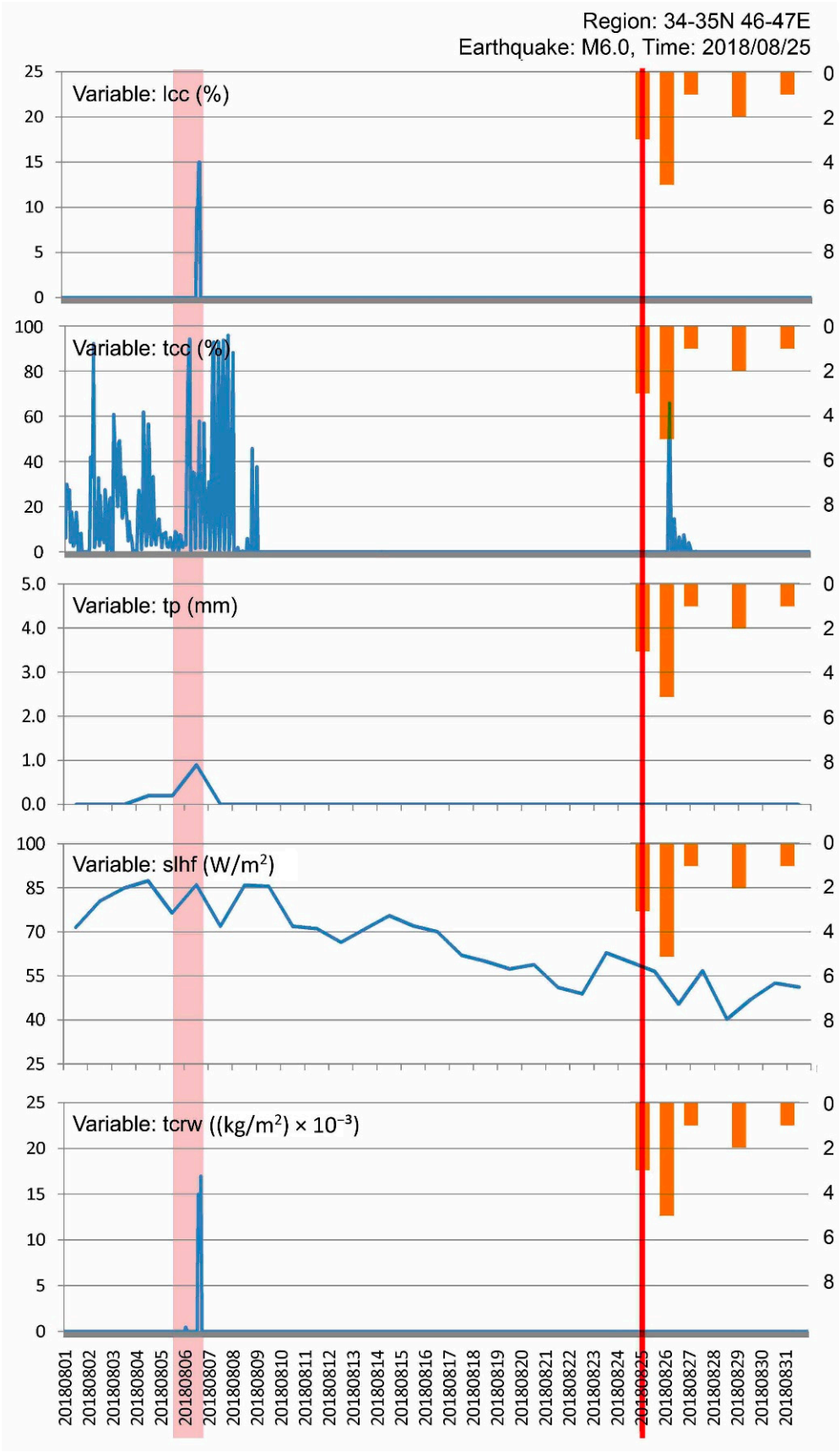

Figure 12. Climatic time series of lcc, tcc, tp, slhf, and tcrw for the M6.0 earthquake on 25 August 2018 in its seismological region (34–35° N, 46–47° E).

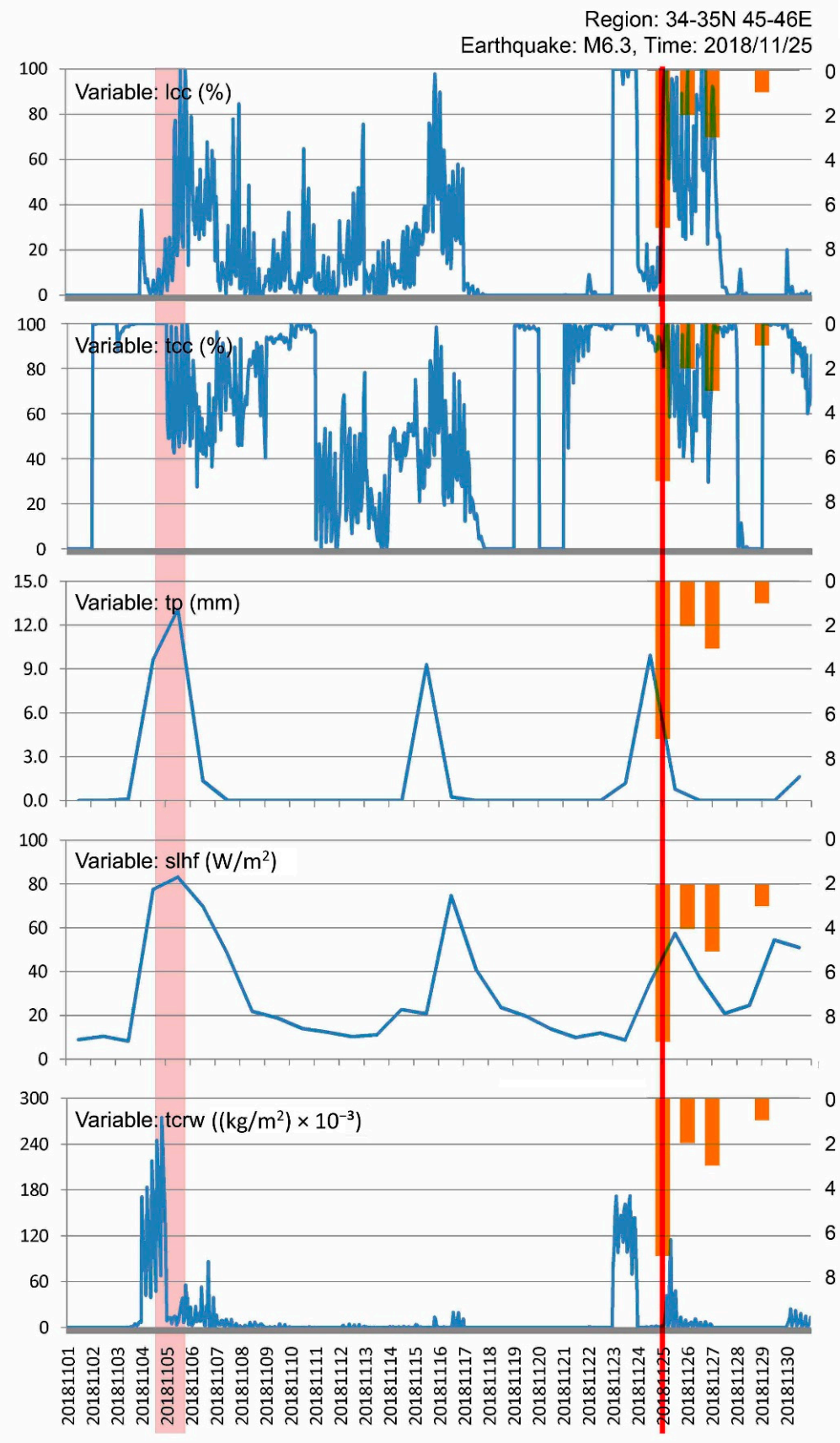

Figure 13. Climatic time series of lcc, tcc, tp, slhf, and tcrw for the M6.3 earthquake on 25 November 2018 in its seismological region (34–35° N, 45–46° E).

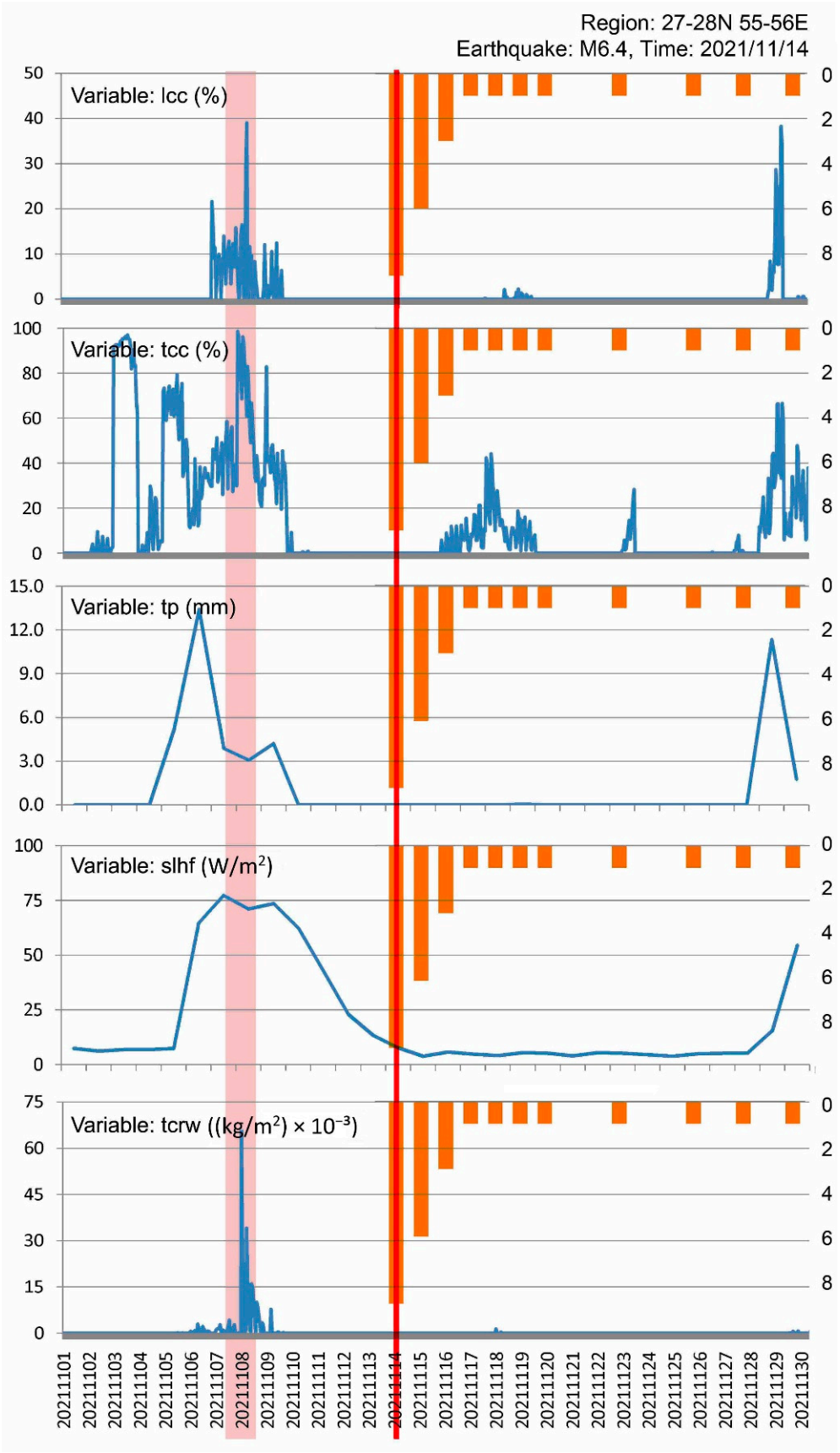

Figure 14. Climatic time series of lcc, tcc, tp, slhf, and tcrw for the M6.4 earthquake on 14 November 2021 in its seismological region (27–28° N, 56–57° E).

Table 3. Mean diurnal values of 5 climatic variables in the given preceding time point (date) and preceding time intervals (days) before the major earthquakes over the epicenter locations (pixels).

Earthquake Date	Spatial Pixel	Preceding Date	Preceding Time (day)	tcc (%)	lcc (%)	tp (mm)	slhf (W/m^2)	tcrw (kg^{-3}/m^2)
27 January 2011	28–29° N, 59–60° E	19 January 2011	9	100	90	9.5	50	150
11 August 2012	38–39° N, 46–47° E	30 July 2012	12	90	50	4.6	110	120
9 April 2013	28–29° N, 51–52° E	6 April 2013	3	90	90	7.2	240	25
16 April 2013	28–29° N, 61–62° E	8 April 2013	8	100	100	12.9	130	90
11 May 2013	26–27° N, 57–58° E	27 April 2013	14	100	10	6.2	250	240
18 August 2014	32–33° N, 47–48° E	18 August 2014	1	100	25	1.1	20	30
5 April 2017	35–36° N, 60–61° E	21 March 2017	15	100	100	12.1	110	10
12 November 2017	34–35° N, 45–46° E	6 November 2017	6	90	40	9.6	50	80
1 December 2017 12 December 2017	30–31° N, 57–58° E	23 November 2017	8 19	100	70	4.1	50	20
25 August 2018	34–35° N, 46–47° E	6 August 2018	20	90	15	0.9	90	15
25 November 2018	34–35° N, 45–46° E	5 November 2018	20	100	100	13.1	80	275
14 November 2021	27–28° N, 56–57° E	8 November 2021	6	100	40	13.4	80	65
Mean	-	-	-	95	60	8.0	105	95

Fully spelled out headings: tcc: total cloud cover; lcc: low cloud cover; tp: total precipitation; slhf: surface latent heat flux; tcrw: total column rain water.

As the climatic values for these earthquakes show, the mean values of tcc, lcc, tp, slhf, and tcrw increased by 100%, 70%, 4.1 mm, 50 W/m^2, and 20 kg^{-3}/m^2, respectively, indicating increases by 95%, 60%, 8.0 mm, 105 W/m^2, and 95 kg^{-3}/m^2, respectively, while the reference values for the aforementioned variables indicated only 25%, 20%, 1.2 mm, 35 W/m^2, and 25 kg^{-3}/m^2, respectively. Therefore, the climatic parameters provide valid precursory information for major earthquakes in Iran within ~20 days and with values that were anomalously high by as much as four times the reference values.

4.3. Estimation of the AUC Index

In this section, the ROC plots for determining the spatial correlations between climatic variables and earthquake events are addressed using the AUC indices. The scatter maps for all climatic variables were produced in GIS based on the known earthquake dates as discussed in the preceding sections. The AUC values for assessing the sensitivity/specificity between climatic variables and impending earthquakes (within ~30 days) are plotted here to show the relative discriminations (Table 4).

Based on the ROC plots for the relation between the times of earthquake events and the test climatic variables, i.e., tcc, lcc, tp, slhf, and tcrw, the calculated AUC indices were found to be equal to 0.677 (tcc), 0.678 (lcc), 0.708 (tp), 0.773 (slhf), and 0.810 (tcrw), indicating an acceptable-to-excellent discrimination (i.e., AUC > 0.6). This means that these scatter values may be used to recognize the arrival of major earthquakes. The ROC plots for the mean AUC values, from 0.677 (tcc) to 0.810 (tcrw), are shown in Figure 15.

Table 4. AUC values for assessing the sensitivity/specificity of climatic variables with respect to impending earthquakes within 30 days, based on the ROC method analysis.

Earthquake Date	tcc	lcc	tp	slhf	tcrw
27 January 2011	0.688	0.835	0.938	0.898	0.875
11 August 2012	0.535	0.650	0.562	0.637	0.688
9 April 2013	0.624	0.667	0.750	0.821	0.833
16 April 2013	0.610	0.733	0.625	0.768	0.750
11 May 2013	0.603	0.557	0.729	0.755	0.829
18 August 2014	0.857	0.729	0.901	0.938	0.929
5 April 2017	0.778	0.556	0.500	0.598	0.667
12 November 2017	0.825	0.629	0.700	0.815	0.800
12 December 2017	0.771	0.700	0.915	0.923	0.917
25 August 2018	0.586	0.614	0.514	0.618	0.928
25 November 2018	0.612	0.721	0.700	0.833	0.828
14 November 2021	0.635	0.750	0.660	0.667	0.677
Mean	0.677	0.678	0.708	0.773	0.810

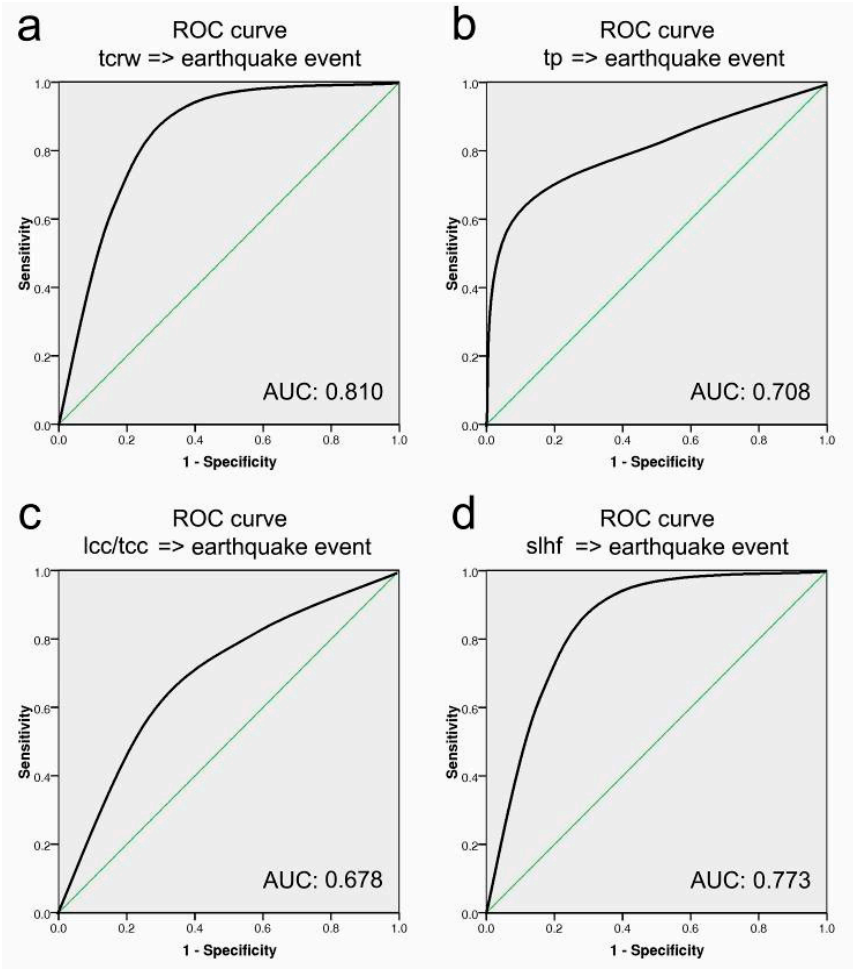

Figure 15. ROC plots for the sensitivity/specificity analysis between earthquake events and climatic variables: (**a**) tcrw; (**b**) tp; (**c**) lcc/tcc; (**d**) slhf.

From the viewpoint of the different seismological regions of Iran, the highest values of the mean AUC indices are observed in the Kerman and Zagros regions, while the lowest

values are observed in the Alborz, Kopet Dag, and Makran regions. This means that the Kerman and Zagros regions provide the best discrimination, concerning the climatic indicators before major earthquakes. This fact could explain why the reported anomalies before earthquakes in these regions appear to be more reliable than those observed in the other parts of Iran. The maps of tcrw (total column perceptible water), which has the highest AUC value relative to the other variables, are presented in Figures 16–18. They provide a visualization of the fact that there seem to be "good areas" and "not-so-good areas" for forecasting major earthquake events in Iran.

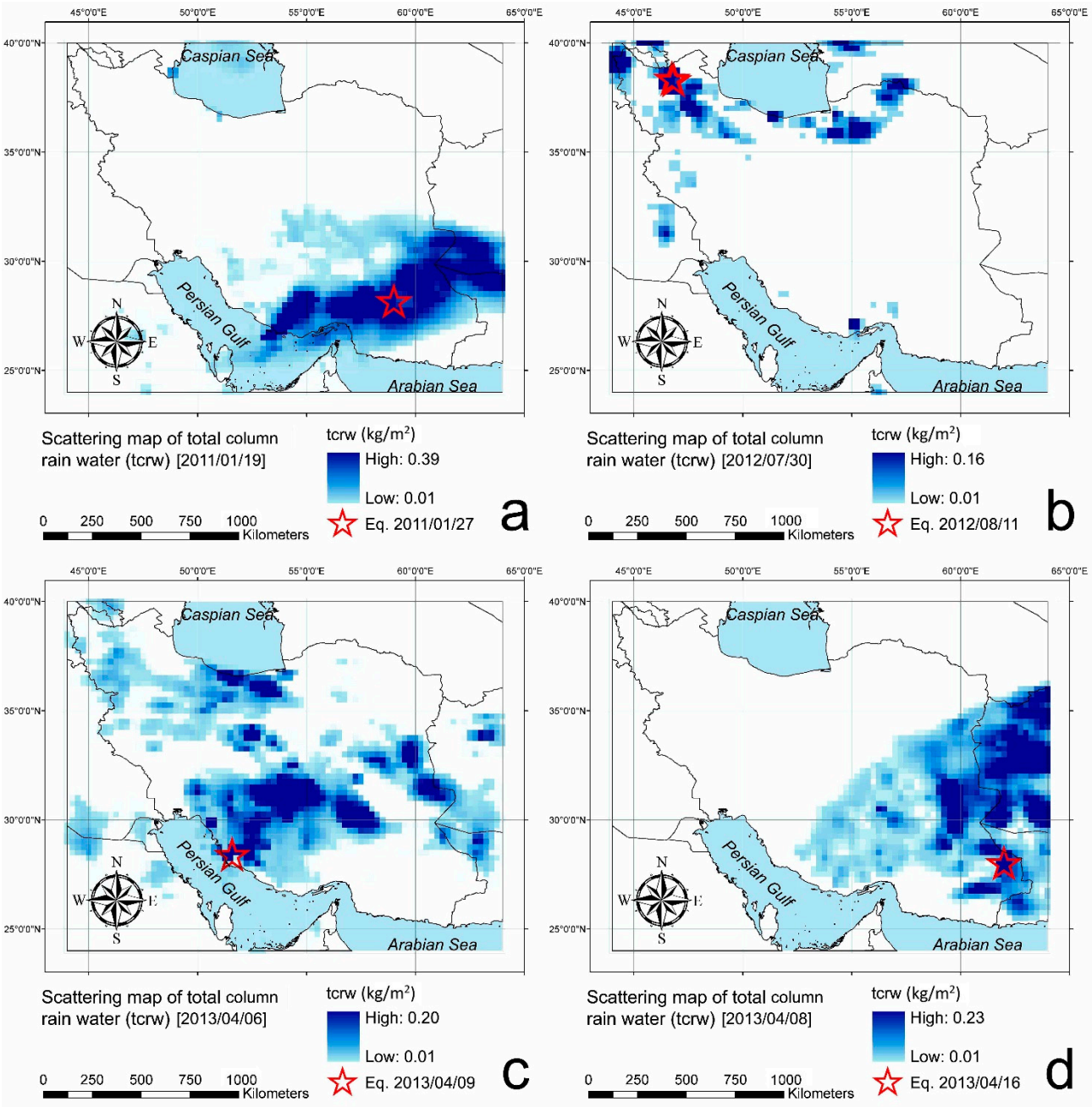

Figure 16. The scattering map of tcrw for the preceding dates before the major earthquakes for (**a**) preceding date of 19 January 2011 before M6.2 earthquake on 27 January 2011; (**b**) preceding date of 30 July 2012 before M6.4 earthquake on 11 August 2012; (**c**) preceding date of 6 April 2013 before M6.4 earthquake on 9 April 2013; (**d**) preceding date of 8 April 2013 before M7.7 earthquake on 16 April 2013.

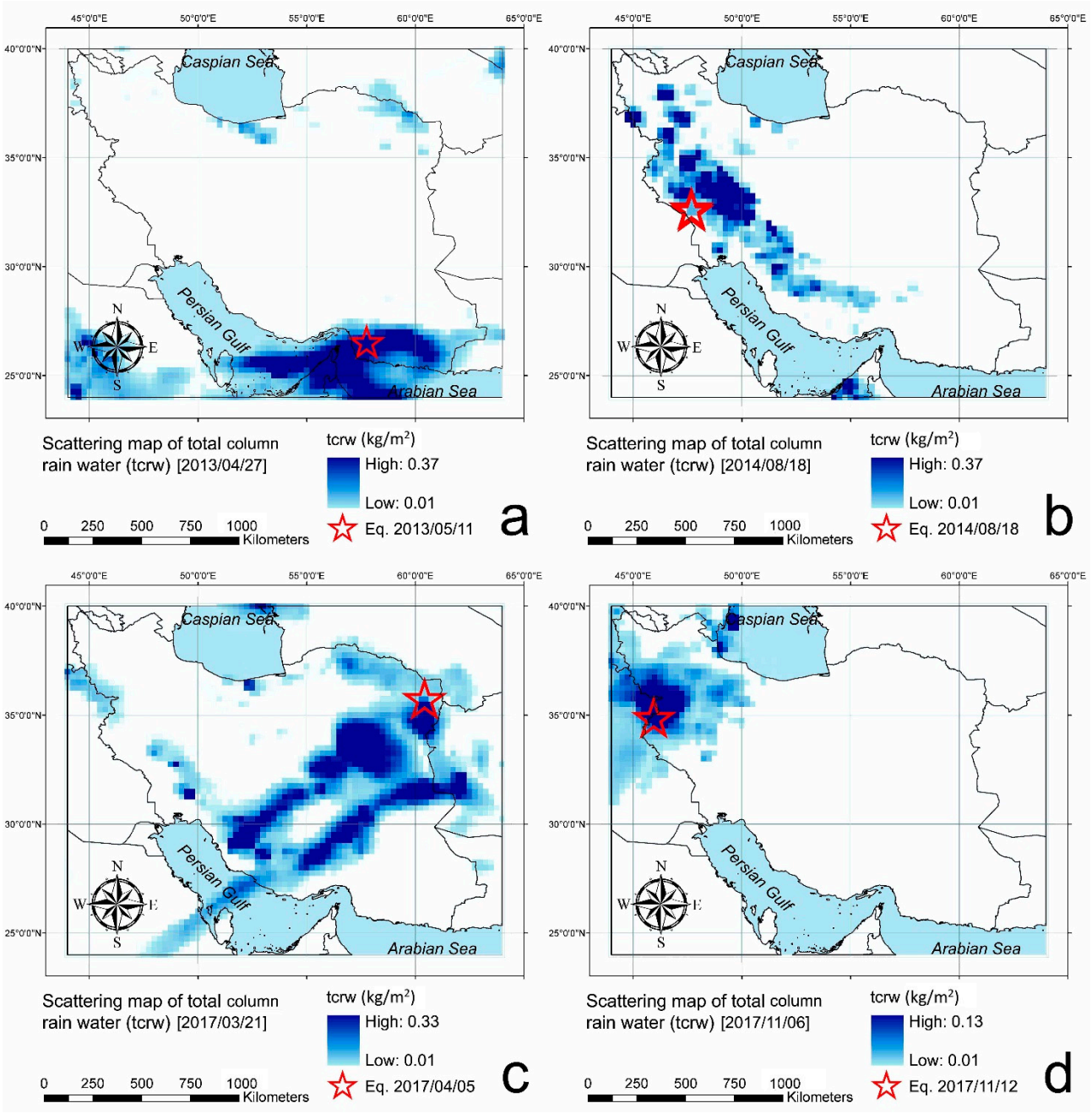

Figure 17. The scattering map of tcrw for the preceding dates before the major earthquakes for (**a**) preceding date of 27 April 2013 before M6.1 earthquake on 11 May 2013; (**b**). preceding date of 18 August 2014 before M6.2 earthquake on 18 August 2014; (**c**) preceding date of 21 March 2017 before M6.1 earthquake on 5 April 2014; (**d**) preceding date of 6 November 2017 before M7.3 earthquake on 12 November 2017.

Air ionization and water condensation were recognized as the basis of short-term latent heat release, increased precipitation, and cloud formation before major earthquakes (e.g., [15,60]). Researchers determined that, before earthquakes, the latent heat flux intensifies, more clouds form, and the rate of precipitation increases [37,40]. The underlying reason is the activation of highly mobile positive holes charge carriers by the increase in dynamic stresses inside the Earth's crust and the migration of these charge carriers to the Earth's surface, where they give rise to several follow-up reactions [14].

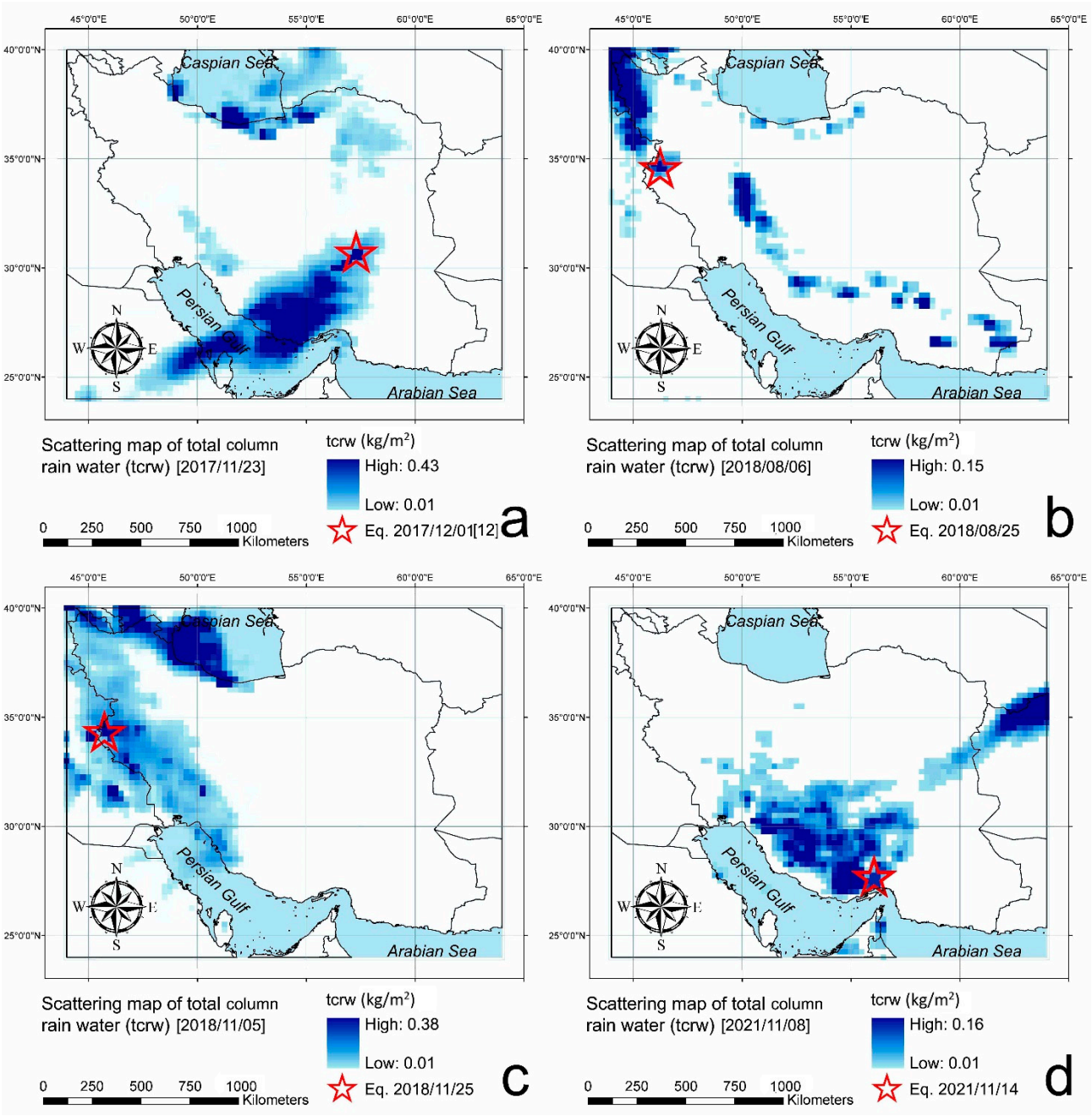

Figure 18. The scattering map of tcrw for the preceding dates before the major earthquakes for (**a**) preceding date of 23 November 2017 before M6.1 (M6.0) earthquake on 1 December 2017 (12 December 2017); (**b**) preceding date of 6 August 2018 before M6.0 earthquake on 25 August 2018; (**c**) preceding date of 5 November 2018 before M6.3 earthquake on 25 November 2018; (**d**) preceding date of 8 November 2021 before M6.4 earthquake on 14 November 2021.

4.4. Examination of Accuracy

In this section, we decided to examine the accuracy of the results, which were determined in the abovementioned parts. For this purpose, a recent destructive earthquake in Türkiye (Turkey) was further investigated. The M7.8 and M7.5 Kahramanmaraş earthquake sequence, with ~10 km focal depth, occurred on 6 February 2023 along the East Anatolian Fault in the seismological region of 37–38° N, 37–38° E. Based on our research method, the preceding date was estimated on 16 January 2023, with a time interval of ~20 days before the main shock, confirming our findings of time lags before major earthquakes in Iran during 2011–2021. The mean climatic values for this earthquake revealed sudden

increases in tcc, lcc, tp, slhf, and tcrw by 100%, 100%, 8.5 mm, 85 W/m^2, and 30 kg^{-3}/m^2, respectively. In addition to the increasing anomalies of the climatic variables in the time series (e.g., the tcrw variation in Figure 19c), the spatial map of variations at the regional level revealed the well-recognized hot spots for the locations of impending M7.8 and M7.5 earthquakes, for the exact preceding and earthquake dates. The scattering maps of tcrw for the preceding date (16 January 2023) and earthquake date (6 February 2023) are shown in Figure 19a,b, respectively. This examination can confirm the overall accuracy of the research method and results. Hence, we can declare that monitoring climatic anomalies and detecting atmospheric signals, particularly the variation of tcrw and its derivations in the time series and spatial expansion, could help us to initially forecast impending major earthquakes at least ~20 days before the possible events. This forecasting system could be established in some populated megacities of Iran, Türkiye, and other Middle Eastern countries, which are located along natural disaster routes.

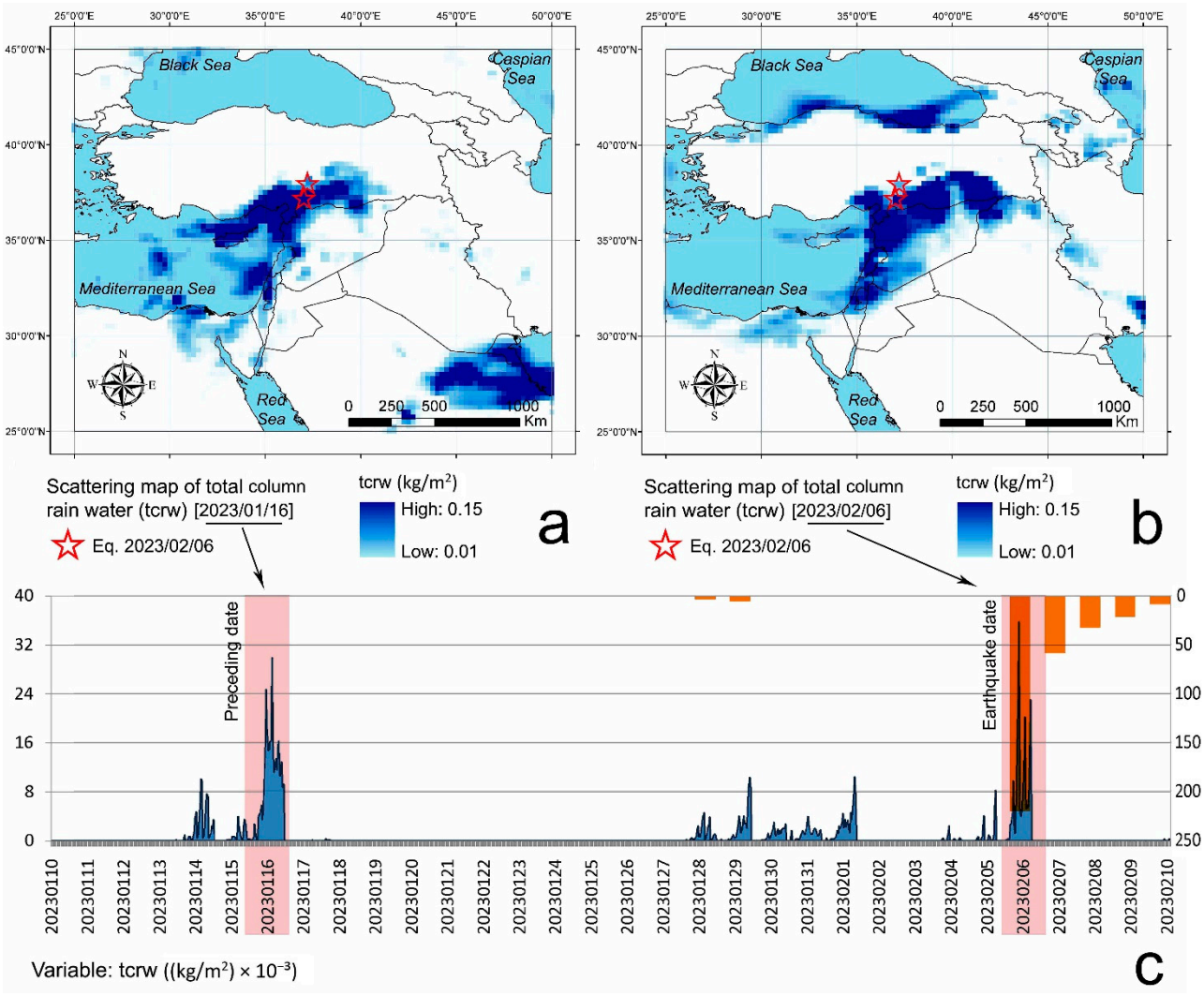

Figure 19. The scattering map of tcrw (**a**) for the preceding date (16 January 2023) before the major earthquakes of M7.8 and M7.5; (**b**) on earthquake date (6 February 2023); (**c**) temporal variation of tcrw for the earthquakes on 6 February 2023 in their seismological region (37–38° N, 37–38° E).

4.5. Underlying Mechanism concerning the Linkages between the Earthquake Events and Pre-Earthquake Anomalies

A literature review concerning the linkages between the atmospheric environment and earthquake events revealed a volume of reports of precursory phenomena such as variations of the precipitation rate, thermal infrared radiation, air temperature, latent heat

flux, and outgoing long wave radiation [20,35]. Previously, scholars, e.g., [61], noted the feedback mechanisms between lithospheric activities and atmospheric dynamics. Therefore, the lithosphere–atmosphere–ionosphere coupling (LAIC) model, developed by Pulinets et al. ([17,22]), demonstrated the existence of geophysical anomalies prior to major earthquakes. However, there is still no consensus about the physical processes linking earthquake precursors [32]. Two types of physical processes were proposed to explain these linkages, including the release of radon from the ground (e.g., [15,62]) and the stress activation of the positive-hole charge carriers within the hypocentral volume and the field ionization of the air at the ground-to-air interface [8,9].

An earthquake commences when tectonic forces subject rocks beneath the lithosphere to increasing levels of mechanical stress. The challenge is to understand how the stressing of rocks inside the Earth's crust can translate into atmospheric and ionospheric anomalies above the Earth's surface [20]. One response to this challenge depends on a coupling mechanism based on the stress activation of peroxy defects in the rocks [9,63]. Peroxy defects are ubiquitous in most rocks, though their presence has not yet been widely noted by the geoscience community. They consist of pairs of oxygen anions, for example, O_3Si-OO-SiO_3, which have each one electron less than the common oxidation state of O^{2-}. Peroxy defects derive from small amounts of solute "water", typically O_3Si-OH, which become incorporated into the matrix of rock-forming minerals, nominally, anhydrous minerals, at the temperature of crystallization from any H_2O-laden magmas or during recrystallization in an H_2O-laden high-grade metamorphic environment. In this case, peroxy defects form along and across grain–grain contacts, making them especially susceptible to activation by mechanical stresses [63]. Deformation of the Si-OO-Si bonds generates electron-hole pairs (e') trapped in the broken peroxy bonds, whereas the holes (h*) turn into highly mobile electronic charge carriers, namely, "positive holes" [9].

During the earthquake preparation phase, the tectonic stresses deep below increase, and the number of positive holes accordingly increases, arriving at the ground-to-air interfaces. When their number density exceeds some threshold value, the local electric fields become strong enough to field-ionize gas molecules, which was demonstrated in laboratory experiments [8,64] and confirmed in the field [65]. Positive holes recombine to form peroxy bonds by an exothermal reaction, which leads to highly excited vibrational states, creating infrared emissions in the thermal infrared bands [66]. Due to the Coulomb repulsion between the positively charged air ions, the ionization pulses propagate outward and upward, leading to ionospheric perturbations such as atmospheric gravity waves (AGW) as the result of the vertical motion of the air mass from the Earth's surface [67–70]. This situation, due to the Coulomb explosion of the heavily ion-laden air, would generate strong vertical winds and follow the atmospheric anomalies described by researchers [20,35].

Overall, field ionization, followed by positive-hole carries at the ground-to-air interface, produce exclusively positive airborne ions, instabilities in the atmosphere, higher electric fields, and the triggering process of corona discharges [8]. In the case of pre-earthquake precursors, ground-ionized air effectively rises, leading to the formation of cluster-ion aerosols, moisture condensation, heavy rainfall, and identifiable ionospheric perturbations, possibly due to electrostatic imbalance. This mechanism can also explain the moisture condensation in the air, air convection patterns, and precipitation occurrences [3,35].

5. Conclusions

Using major earthquake events in Iran during the decade of 2011–2021, the present study provides a systematic assessment of the various factors that control a wide range of climatic variables that tend to produce anomalous values during the time window of approximately only 30 days before the main shocks. Based on daily data and a geographical grid of $1^\circ \times 1^\circ$, the multidimensional NetCDF files of the ERA5 database were used to estimate the changes in the climatic variables within the study area. A special methodology was used to investigate the relationship between climatic variables and major earthquake

events within 30 days before the main shocks, using the combination of a cross-correlation function (CCF) and receiver operating characteristic (ROC).

The CCF plots reached maximum values ranging from 0.42 to 0.92. They indicate that the increase in certain climatic parameters, such as precipitation and the Earth's surface latent heat flux, can be used to forecast earthquake activity 8 days and 20 days prior to major seismic events, thereby achieving the high possibility ($p > 90\%$) of a successful forecast. In addition, the ROC plots indicate that the AUC indices from 0.677 (tcc) to 0.810 (tcrw) in the recognized preseismic times provide for an acceptable-to-excellent correlation between earthquake events and pre-earthquake climatic variables. Furthermore, when graphically evaluated, the results show that the hot spots are well-correlated with the locations of impending major earthquakes.

The results presented here have managerial implications for operating earthquake forecast systems in Iran and other Middle Eastern countries. To reach this goal, a systematic methodology was developed that can be used to analyze the findings in similar seismically active regions such as Türkiye and Pakistan. The main contribution of the present study may arise from the recognition that a relationship exists between climatic variables and earthquake events (see Daneshvar et al. [44]). While the previous work was based on only two climatic variables, e.g., precipitation and temperature, this study used a broader set of climatic variables from a multidimensional global dataset (ERA5).

In addition, another implication of the work presented here is the demonstration of the usefulness of a methodology, namely, the use of a cross-correlation function (CCF) and a receiver operating characteristic (ROC) to develop spatial and temporal analytics. The results can help national and regional governments establish earthquake forecast systems with potentially far-reaching economic and humanitarian implications, in comparison to the anticipated earthquake damages and losses. As mentioned by renowned scientists in the field such as Mignan et al. [4] and Hakayawa et al. [71], national and regional governments should be made aware of the earthquake forecast system presented here, which is based on the analysis of correlations between climatic variables and short-term pre-earthquake signals. In the present study, we considered the relations between climatic variables and major earthquakes ($M > 6$) within the time series (~30 days) only before the main shocks. As a recommendation for research in the future, (i): the research on the variations after the main shocks certainly needs a further attempt; (ii): a possible relation between the magnitude of the earthquake events and the precursor time of the appearance of climatic anomalies can be studied; and (iii): the research on the atmospheric anomalies before smaller earthquake events (i.e., $M < 6$) can be helpful for our earthquake forecasting knowledge.

Author Contributions: Conceptualization, M.R.M.D. and F.T.F.; methodology, M.R.M.D. and F.T.F.; software, M.R.M.D.; validation, M.R.M.D., F.T.F. and M.E.; formal analysis, M.R.M.D. and M.E.; investigation, M.R.M.D. and F.T.F.; resources, M.R.M.D. and F.T.F.; data curation, M.R.M.D. and M.E.; writing—original draft preparation, M.R.M.D. and M.E.; writing—review and editing, M.R.M.D. and F.T.F.; visualization, M.R.M.D. and M.E.; supervision, F.T.F.; project administration, F.T.F. All authors have read and agreed to the published version of the manuscript.

Funding: This research received no external funding.

Informed Consent Statement: Informed consent was obtained from the individual participants included in the study.

Data Availability Statement: The data that support the findings of this study are available from the corresponding author upon request.

Acknowledgments: We wish to acknowledge the Copernicus Climate Change Service (C3S) and Climate Data Store (CDS) (https://cds.climate.copernicus.eu/cdsapp#!/home, acsessed on 20 December 2022) for providing the reanalysis data of the global climate.

Conflicts of Interest: The authors declare no conflict of interest.

Abbreviations

AGW: atmospheric gravity waves; AUC: area under the curve; CCF: cross-correlation function; ERA5: European Centre for Medium-Range Weather Forecasts reanalysis data version 5; GIS: geographical information system; NetCDF: network common data form; ROC: receiver operating characteristic; SPSS: Statistical Package for Social Sciences; lcc: low cloud cover; slhf: surface latent heat flux; tcc: total cloud cover; tcrw: total column rainwater; tp: total precipitation.

References

1. Qin, K.; Guo, G.M.; Wu, L.X. Surface latent heat flux anomalies preceding inland earthquakes in China. *Earthq. Sci.* **2009**, *22*, 555–562. [CrossRef]
2. Qin, K.; Wu, L.X.; De Santis, A.; Meng, J.; Ma, W.Y.; Cianchini, G. Quasi-synchronous multi-parameter anomalies associated with the 2010–2011 New Zealand earthquake sequence. *Nat. Hazards Earth Syst. Sci.* **2012**, *12*, 1059–1072. [CrossRef]
3. Daneshvar, M.R.M.; Freund, F.T. Survey of a relationship between precipitation and major earthquakes along the Peru-Chilean trench (2000–2015). *Eur. Phys. J. Spec. Top.* **2021**, *230*, 335–351. [CrossRef]
4. Mignan, A.; Ouillon, G.; Sornette, D.; Freund, F.T. Global earthquake forecasting system (GEFS): The challenges ahead. *Eur. Phys. J. Spec. Top.* **2021**, *230*, 473–490. [CrossRef]
5. Parrot, M.; Tramutoli, V.; Liu, T.J.Y.; Pulinets, S.; Ouzounov, D.; Genzano, N.; Lisi, M.; Hattori, K.; Namgaladze, A. Atmospheric and ionospheric coupling phenomena associated with large earthquakes. *Eur. Phys. J. Spec. Top.* **2021**, *230*, 197–225. [CrossRef]
6. Marchitelli, V.; Harabaglia, P.; Troise, C.; De Natale, G. On the correlation between solar activity and large earthquakes worldwide. *Sci. Rep.* **2020**, *10*, 11495. [CrossRef]
7. Freund, F.T. Earthquake Forewarning—A Multidisciplinary Challenge from the Ground up to Space. *Acta Geophys.* **2013**, *61*, 775–807. [CrossRef]
8. Freund, F.T.; Kulahci, I.G.; Cyr, G.; Ling, J.; Winnick, M.; Tregloan-Reed, J.; Freund, M.M. Air ionization at rock surfaces and pre-earthquake signals. *J. Atmos. Sol. Terr. Phys.* **2009**, *71*, 1824–1834. [CrossRef]
9. Freund, F.T.; Freund, M.M. Paradox of Peroxy Defects and Positive Holes in Rocks Part I: Effect of Temperature. *J. Asian Earth Sci.* **2015**, *114*, 373–383. [CrossRef]
10. Pulinets, S.A.; Ouzounov, D.; Karelin, A.V.; Davidenko, D.V. Physical bases of the generation of short-term earthquake precursors: A complex model of ionization-induced geophysical processes in the lithosphere-atmosphere-ionosphere magnetosphere system. *Geomagn. Aeron.* **2015**, *55*, 521–538. [CrossRef]
11. Pulinets, S.A.; Ouzounov, D. *The Possibility of Earthquake Forecasting: Learning from Nature*; IOP Publishing: Bristol, UK, 2018; p. 167. [CrossRef]
12. Ching-Chou, F.; Walia, V.; Yang, T.F.; Lou-Chuang, L.; Liu, T.K.; Cheng-Hong, C.; Kumar, A.; Shih-Jung, L.; Lai, T.H.; Kuo-Liang, W. Preseismic anomalies in soil-gas radon associated with 2016 M 6.6 Meinong earthquake, Southern Taiwan. *Terr. Atmos. Ocean. Sci.* **2017**, *28*, 7. [CrossRef]
13. Fu, C.C.; Lee, L.C.; Yang, T.F.; Lin, C.H.; Chen, C.H.; Walia, V.; Liu, T.K.; Ouzounov, D.; Giuliani, G.; Lai, T.H.; et al. Gamma ray and radon anomalies in northern Taiwan as a possible preearthquake indicator around the plate boundary. *Geofluids* **2019**, *2019*, 4734513. [CrossRef]
14. Freund, F.T.; Ouillon, G.; Scoville, J.; Sornette, D. Earthquake precursors in light of the peroxy defect theory: Critical review of systematic observations. *Eur. Phys. J. Spec. Top.* **2021**, *230*, 7–46. [CrossRef]
15. Pulinets, S.A.; Ouzounov, D.; Karelin, A.V.; Boyarchuk, K.A.; Pokhmelnykh, L.A. The physical nature of thermal anomalies observed before strong earthquakes. *Phys. Chem. Earth* **2006**, *31*, 143–153. [CrossRef]
16. Ouzounov, D.; Liu, D.; Chunli, K.; Cervone, G.; Kafatos, M.; Taylor, P. Outgoing long wave radiation variability from IR satellite data prior to major earthquakes. *Tectonophysics* **2007**, *431*, 211–220. [CrossRef]
17. Pulinets, S.A.; Ouzounov, D. Lithosphere-atmosphere-ionosphere coupling (LAIC) model: An unified concept for earthquake precursors validation. *J. Asian Earth Sci.* **2011**, *41*, 371–382. [CrossRef]
18. Hayakawa, M.; Hobara, Y.; Rozhnoi, A.; Solovieva, M.; Ohta, K.; Izutsu, J.; Nakamura, T.; Kasahara, Y. The ionospheric precursor to the 2011 March 11 earthquake based upon observations obtained from the Japan-Pacific subionospheric VLF/LF network. *Terr. Atmos. Ocean. Sci.* **2013**, *24*, 393–408. [CrossRef]
19. Hakayawa, M. *Earthquake Prediction with Radio Techniques*; John Wiley & Sons: Singapore, 2015. [CrossRef]
20. Daneshvar, M.R.M.; Freund, F.T. Remote Sensing of Atmospheric and Ionospheric Signals Prior to the Mw 8.3 Illapel Earthquake, Chile 2015. *Pure Appl. Geophys.* **2017**, *174*, 11–45. [CrossRef]
21. Hayakawam, M.; Asano, T.; Rozhnoi, A.; Solovieva, M. VLF/LF sounding of ionospheric perturbations and possible association with earthquakes. In *Pre-Earthquake Processes: A Multidisciplinary Approach to Earthquake Prediction Studies*; Ouzounov, D., Pulinets, S., Hattori, K., Taylor, P., Eds.; American Geophysical Union: Washington, DC, USA, 2018; pp. 277–304. [CrossRef]

22. Pulinets, S.A.; Ouzounov, D.; Karelin, A.; Davidenko, D.V. Lithosphere-atmosphere-ionosphere-magnetosphere coupling—A concept for pre-earthquake signals generation. In *Pre-Earthquake Processes: A Multi-Disciplinary Approach to Earthquake Prediction Studies*; American Geophysical Union: Washington, DC, USA, 2018; pp. 79–98. Available online: https://digitalcommons.chapman.edu/scs_books/44 (accessed on 25 January 2020).
23. Ouzounov, D.; Pulinets, S.; Liu, J.Y.; Hattori, K.; Han, P. Multiparameter assessment of pre-earthquake atmospheric signals. In *Pre-Earthquake Processes: A Multidisciplinary Approach to Earthquake Prediction Studies*; Ouzounov, D., Pulinets, D., Hattori, K., Taylor, P., Eds.; American Geophysical Union: Washington, DC, USA; John Wiley & Sons, Inc.: Hoboken, NJ, USA, 2018; pp. 339–359. [CrossRef]
24. Shah, M.; Jin, S. Pre-seismic ionospheric anomalies of the 2013 Mw = 7.7 Pakistan earthquake from GPS and COSMIC observations. *Geod. Geodyn.* **2018**, *9*, 378–387. [CrossRef]
25. Tariq, M.A.; Shah, M.; Pajares, M.H.; Iqbal, T. Pre-earthquake ionospheric anomalies before three major earthquakes by GPS-TEC and GIM-TEC data during 2015–2017. *Adv. Space Res.* **2019**, *63*, 2088–2099. [CrossRef]
26. Yang, S.S.; Asano, T.; Hayakawa, M. Abnormal gravity wave activity in the stratosphere prior to the 2016 Kumamoto earthquakes. *J. Geophys. Res. Space Phys.* **2019**, *124*, 1410–1425. [CrossRef]
27. Akhoondzadeh, M.; De Santis, A.; Marchetti, D.; Piscini, A.; Jin, S. Anomalous seismo-LAI variations potentially associated with the 2017 Mw=7.3 Sarpol-e Zahab (Iran) earthquake from Swarm satellites, GPS-TEC and climatological data. *Adv. Space Res.* **2019**, *64*, 143–158. [CrossRef]
28. De Santis, A.; Marchetti, D.; Pav'on-Carrasco, F.J.; Cianchini, G.; Perrone, L.; Abbattista, C.; Alfonsi, L.; Amoruso, L.; Campuzano, S.A.; Carbone, M.; et al. Precursory worldwide signatures of earthquake occurrences on swarm satellite data. *Sci. Rep.* **2019**, *9*, 20287. [CrossRef]
29. Shah, M.; Aibar, A.C.; Tariq, M.A.; Ahmed, J.; Ahmed, A. Possible ionosphere and atmosphere precursory analysis related to Mw >6.0 earthquakes in Japan. *Remote Sens. Environ.* **2020**, *239*, 111620. [CrossRef]
30. Marchetti, D.; De Santis, A.; Shen, X.; Campuzano, S.A.; Perrone, L.; Piscini, A.; Di Giovambattista, R.; Jin, S.; Ippolito, A.; Cianchini, G.; et al. Possible lithosphere-atmosphere-ionosphere coupling effects prior to the 2018 Mw=7.5 Indonesia earthquake from seismic, atmospheric and ionospheric data. *J. Asian Earth Sci.* **2020**, *188*, 104097. [CrossRef]
31. Liu, Q.; Shen, X.; Zhang, J.; Cui, J.; Tan, Q.; Zhao, S.; Li, M. Aerosol anomalies associated with occurrence of recent strong earthquakes (>M 8.0). *Terr. Atmos. Ocean. Sci.* **2020**, *31*, 677–689. [CrossRef]
32. Şentürk, E.; Inyurt, S.; Sertçelik, İ. Ionospheric anomalies associated with Mw7.3 Iran-Iraq border earthquake and a moderate magnetic storm. *Ann. Geophys. Discus.* **2020**, *38*, 1031–1043. [CrossRef]
33. Adil, M.A.; Şentürk, E.; Pulinets, S.A.; Mazaudier, C.A. A lithosphere–atmosphere–ionosphere coupling phenomenon observed before M 7.7 Jamaica earthquake. *Pure Appl. Geophys.* **2021**, *178*, 3869–3886. [CrossRef]
34. Zhao, D.; Chen, L.; Yu, Y. Associations between strong earthquakes and local rainfall in China. *Front. Earth Sci.* **2021**, *9*, 760497. [CrossRef]
35. Freund, F.T.; Daneshvar, M.R.M.; Ebrahimi, M. Atmospheric storm anomalies prior to major earthquakes in the Japan region. *Sustainability.* **2022**, *14*, 10241. [CrossRef]
36. De Santis, A.; Perrone, L.; Calcara, M.; Campuzano, S.A.; Cianchini, G.; D'Arcangelo, S.; Mauro, D.D.; Marchetti, D.; Nardi, A.; Orlando, M.; et al. A comprehensive multiparametric and multilayer approach to study the preparation phase of large earthquakes from ground to space: The case study of the June 15 2019, M7.2 Kermadec Islands (New Zealand) earthquake. *Remote Sens. Environ.* **2022**, *283*, 113325. [CrossRef]
37. Ghosh, S.; Chowdhury, S.; Kundu, S.; Sasmal, S.; Politis, D.Z.; Potirakis, S.M.; Hayakawa, M.; Chakraborty, S.; Chakrabarti, S.K. Unusual surface latent heat fluxvariations and their critical dynamics revealed before strong earthquakes. *Entropy* **2022**, *24*, 23. [CrossRef] [PubMed]
38. Khan, M.M.; Ghaffar, B.; Shahzad, R.; Khan, M.R.; Shah, M.; Amin, A.H.; Eldin, S.M.; Naqvi, N.A.; Ali, R. Atmospheric anomalies associated with the 2021 Mw 7.2 Haiti earthquake using machine learning from multiple satellites. *Sustainability* **2022**, *14*, 14782. [CrossRef]
39. Picozza, P.; Conti, L.; Sotgiu, A. Looking for earthquake precursors from space: A critical review. *Front. Earth Sci.* **2021**, *9*, 676775. [CrossRef]
40. Daneshvar, M.R.M.; Khosravi, M.; Tavousi, T. Seismic triggering of atmospheric variables prior to the major earthquakes in the Middle East within a 12-year time-period of 2002–2013. *Nat. Hazards* **2014**, *74*, 1539–1553. [CrossRef]
41. Daneshvar, M.R.M.; Tavousi, T.; Khosravi, M. Synoptic detection of the short-term atmospheric precursors prior to a major earthquake in the Middle East, North Saravan M 7.8 earthquake, SE Iran. *Air. Qual. Atmos. Health* **2014**, *7*, 29–39. [CrossRef]
42. Daneshvar, M.R.M.; Tavousi, T.; Khosravi, M. Atmospheric blocking anomalies as the synoptic precursors prior to the induced earthquakes; A new climatic conceptual model. *Int. J. Environ. Sci. Technol.* **2015**, *12*, 1705–1718. [CrossRef]
43. Daneshvar, M.R.M.; Freund, F.T. Examination of a relationship between atmospheric blocking and seismic events in the Middle East using a new seismo-climatic index. *Swiss J. Geosci.* **2019**, *112*, 435–451. [CrossRef]
44. Daneshvar, M.R.M.; Freund, F.T.; Ebrahimi, M. Time-lag correlations between atmospheric anomalies and earthquake events in Iran and the surrounding Middle East region (1980–2018). *Arab. J. Geosci.* **2021**, *14*, 1210. [CrossRef]
45. Daneshvar, M.R.M.; Bagherzadeh, A.; Tavousi, T. Assessment of bioclimatic comfort conditions based on Physiologically Equivalent Temperature (PET) using the RayMan Model in Iran. *Cent. Eur. Geol.* **2013**, *5*, 53–60. [CrossRef]

46. Fick, S.E.; Hijmans, R.J. WorldClim 2: New 1 km spatial resolution climate surfaces for global land areas. *Int. J. Climatol.* **2017**, *37*, 4302–4315. [CrossRef]
47. Daneshvar, M.R.M.; Ebrahimi, M.; Nejadsoleymani, H. Investigation of mining-induced earthquakes in Iran within a time window of 2006–2013. *J. Seismol.* **2018**, *22*, 1437–1450. [CrossRef]
48. USGS. Earthquake Archive Data. Online Catalog of United States Geological Survey. Available online: https://earthquake.usgs.gov/earthquakes/search (accessed on 20 December 2022).
49. Hersbach, H.; Bell, B.; Berrisford, P.; Biavati, G.; Horányi, A.; Muñoz Sabater, J.; Nicolas, J.; Peubey, C.; Radu, R.; Rozum, I.; et al. ERA5 hourly data on single levels from 1959 to present. In *European Copernicus Climate Change Service and Climate Data Store*; European Meteorological Society: Berlin, Germany, 2018. [CrossRef]
50. Daneshvar, M.R.M.; Ebrahimi, M.; Nejadsoleymani, H.; Mahmoudzadeh, A. Investigation of a seismic teleconnection model between Iran and Iceland regions during 1980–2018. *Model. Earth Syst. Environ.* **2020**, *6*, 2215–2224. [CrossRef]
51. Probst, W.N.; Stelzenmüller, V.; Ove Fock, H. Using cross-correlations to assess the relationship between time-lagged pressure and state indicators: An exemplary analysis of North Sea fish population indicators. *ICES J. Mar. Sci.* **2012**, *69*, 670–681. [CrossRef]
52. Straile, D.; Eckmann, R.; Juengling, T.; Thomas, G.; Loeffler, H. Influence of climate variability on whitefish (Coregonus lavaretus) year-class strength in a deep, warm monomictic lake. *Oecologia* **2007**, *151*, 521–529. [CrossRef] [PubMed]
53. Greenstreet, S.P.R.; Rogers, S.I.; Rice, J.C.; Piet, G.J.; Guirey, E.J.; Fraser, H.M.; Fryer, R.J. Development of the EcoQO for the North Sea fish community. *ICES J. Mar. Sci.* **2011**, *68*, 1–11. [CrossRef]
54. Gröger, J.P.; Fogarty, M.J. Broad-scale climate influences on cod (*Gadus morhua*) recruitment on Georges Bank. *ICES J. Mar. Sci.* **2011**, *68*, 592–602. [CrossRef]
55. Shephard, S.; Reid, D.G.; Greenstreet, S.P.R. Interpreting the large fish indicator for the Celtic Sea. *ICES J. Mar. Sci.* **2011**, *68*, 1963–1972. [CrossRef]
56. Lasko, T.A.; Bhagwat, J.G.; Zou, K.H.; Ohno-Machado, L. The use of receiver operating characteristic curves in biomedical informatics. *J. Biomed. Inform.* **2005**, *38*, 404–415. [CrossRef]
57. Liuzzo, L.; Sammartano, V.; Freni, G. Comparison between different distributed methods for flood susceptibility mapping. *Water Resour. Manag.* **2019**, *33*, 3155–3173. [CrossRef]
58. Pirnia, A.; Darabi, H.; Choubin, B.; Omidvar, E.; Onyutha, C.; Haghighi, A.T. Contribution of climatic variability and human activities to stream flow changes in the Haraz River basin, northern Iran. *J. Hydro-Environ. Res.* **2019**, *25*, 12–24. [CrossRef]
59. Khatami, F.; Vilamová, Š.; Cagno, E.; De Bernardi, P.; Neri, A.; Cantino, V. Efficiency of consumer behaviour and digital ecosystem in the generation of the plastic waste toward the circular economy. *J. Environ. Manag.* **2023**, *325*, 116555. [CrossRef]
60. Piroddi, L.; Ranieri, G.; Freund, F.T.; Trogu, A. Geology, tectonics and topography underlined by L'Aquila earthquake TIR precursors. *Geophys. J. Int.* **2014**, *197*, 1532–1536. [CrossRef]
61. Iaffaldano, G.; Husson, L.; Bunge, H.P. Monsoon speeds up Indian plate motion. *Earth Planet. Sci. Lett.* **2011**, *304*, 503–510. [CrossRef]
62. Hayakawa, M.; Schekotov, A.; Izutsu, J.; Yang, S.S.; Solovieva, M.; Hobara, Y. Multi-parameter observations of seismogenic phenomena related to the Tokyo earthquake (M = 5.9) on 7 October 2021. *Geosciences* **2022**, *12*, 265. [CrossRef]
63. Scoville, J.; Sornette, J.; Freund, F.T. Paradox of peroxy defects and positive holes in rocks Part II: Outflow of electric currents from stressed rocks. *J. Asian Earth Sci.* **2015**, *114*, 338–351. [CrossRef]
64. King, B.V.; Freund, F.T. Surface charges and subsurface space charge distribution in magnesium oxide containing dissolved traces of water. *Phys. Rev. B* **1984**, *29*, 5814–5824. [CrossRef]
65. Bleier, T.; Dunson, C.; Maniscalco, M.; Bryant, N.; Bambery, R.; Freund, F.T. Investigation of ULF magnetic pulsations, air conductivity changes, and infra red signatures associated with the 30 October 2007 Alum Rock M5.4 earthquake. *Nat. Hazards Earth Syst. Sci.* **2009**, *9*, 585–603. [CrossRef]
66. Freund, F.T.; Takeuchi, A.; Lau, B.W.S.; Al-Manaseer, A.; Fu, C.C.; Bryant, N.A.; Ouzounov, D. Stimulated thermal IR emission from rocks: Assessing a stress indicator. *eEarth* **2007**, *2*, 7–16. [CrossRef]
67. Lizunov, G.; Hayakawa, M. Atmospheric Gravity Waves and their Role in the Lithosphere-troposphere-ionosphere Interaction. *IEEJ Trans. Fundam. Mater.* **2004**, *124*, 1109–1120. [CrossRef]
68. Garcia, R.; Crespon, F.; Ducic, V.; Lognonné, P. Three-dimensional ionospheric tomography of post-seismic perturbations produced by the Denali earthquake from GPS data. *Geophys. J. Int.* **2005**, *163*, 1049–1064. [CrossRef]
69. Rozhnoi, A.; Solovieva, M.; Molchanov, O.A.; Biagi, P.F.; Hayakawa, M. Observation evidences of atmospheric Gravity Waves induced by seismic activity from analysis of subionospheric LF signal spectra. *Nat. Hazards Earth Syst. Sci.* **2007**, *7*, 625–628. [CrossRef]
70. Hayakawa, M.; Kasahara, Y.; Nakamura, T.; Hobara, Y.; Rozhnoi, A.; Solovieva, M.; Molchanov, O.A.; Korepanov, V. Atmospheric gravity waves as a possible candidate for seismo-ionospheric perturbations. *J. Atmos. Electr.* **2011**, *31*, 129–140. [CrossRef]
71. Hayakawa, M.; Izutsu, J.; Schekotov, A.; Yang, S.S.; Solovieva, M.; Budilova, E. Lithosphere–atmosphere–ionosphere coupling effects based on multiparameter precursor observations for February–March 2021 earthquakes (m~7) in the offshore of Tohoku area of Japan. *Geosciences* **2021**, *11*, 481. [CrossRef]